

## STABILITY OF NONROTATING STELLAR SYSTEMS. I. OBLATE SHELL-ORBIT MODELS

DAVID MERRITT AND MASSIMO STIAVELLI  
 Department of Physics and Astronomy, Rutgers University  
 Received 1989 September 25; accepted 1990 February 2

### ABSTRACT

We investigate the dynamical stability of nonrotating oblate galaxy models constructed from thin short-axis tube orbits (“shell” orbits). Models as flat or flatter than  $\sim E6$  (axis ratio of  $\sim 2:5$ ) are axisymmetrically unstable and laminate into thin, curved cylinders on roughly an orbital time scale. All shell-orbit models are unstable to a more global, nonaxisymmetric instability with an essentially dipole or “ $m = 1$ ” character, i.e., the perturbed density varies roughly as  $\cos \phi$  around the short axis. The strength of the  $m = 1$  instability decreases with the roundness of the model, but models as round as  $E1$  are still clearly unstable; the spherical model appears to be stable, in agreement with previous analytic and numerical work. The instability is apparent in integrations carried out with two very different  $N$ -body codes: a harmonic-expansion code, in which the accuracy of the integration depends strongly on the choice of grid center at each time step, and a (much slower) “tree” code, which has no preferred center.

Our results imply that oblate stellar systems require a minimum amount of radial kinetic energy to be dynamically stable, even in the absence of net rotation. In the case of models flatter than  $\sim E5$ , the radial velocity dispersions required for stability appear to be quite large, of order  $\frac{1}{4}$  to  $\frac{1}{3}$  the circular velocity.

*Subject headings:* galaxies: internal motions — galaxies: structure — instabilities — stars: stellar dynamics

### I. INTRODUCTION

Since the pioneering work of Toomre, Hunter, Kalnajs, and Hohl, there has been little doubt that dynamical instabilities are crucial to our understanding of the structure and evolution of disk galaxies. By contrast, theoretical work on elliptical galaxies has so far focused on the more narrow problem of constructing exact equilibrium models; questions of stability have mostly been swept under the rug. In part, this neglect can be attributed simply to the difficulty of the self-consistent problem in ellipsoidal geometry. Furthermore, as Antonov (1960, 1962) showed almost 30 years ago, spherical, isotropic stellar systems are generally stable, a result which suggests that pressure-supported galaxies are less prone to instabilities than flattened, rotating ones. This assumption is consistent with the smooth featureless appearance of most elliptical galaxies, an appearance which seems to rule out any ongoing instabilities of the sort that are believed to drive bars or spiral patterns in disk galaxies. However, the possibility remains that dynamical instabilities may be important in constraining the possible equilibrium shapes of elliptical galaxies, or the range of kinematical solutions consistent with a given shape. These instabilities may also play an active role during galaxy formation.

This paper is the first in a series that will systematically investigate the importance of dynamical instabilities in flattened, pressure-supported stellar systems. There are three compelling reasons for undertaking such an investigation at the present time. First, the analytical tools for constructing realistic, two- and three-integral equilibrium models of spheroidal and ellipsoidal galaxies are now largely at hand (Bishop 1986, 1987; Dejonghe 1986, 1987; Dejonghe and de Zeeuw 1988*b*; Evans 1989). Second, the last few years have seen the development of a number of efficient  $N$ -body algorithms that are well suited to evolving models of smooth, flattened systems like elliptical galaxies (as reviewed by Sellwood 1987).  $N$ -body techniques are probably unavoidable when searching for instabilities in nonspherical and nondisk models, because of the

practical difficulties of performing a three-dimensional perturbation analysis; in addition, the nonlinear evolution is generally interesting from an astrophysical point of view. Third, there is some reason to believe that dynamical instabilities are prevalent in nonrotating galaxy models—probably not as ubiquitous as in rotationally supported disks, but very common nevertheless. For instance, spherical models with a mean ratio of radial to tangential velocity dispersions as small as  $\sim 1.4$  are generally bar-unstable (e.g., Merritt and Aguilar 1985). Additional evidence comes from the recent work of Polyachenko and collaborators (summarized in Fridman and Polyachenko 1984) on the stability of idealized stellar systems with various geometries. The Soviet workers find hints that a wide variety of nonspherical, pressure-supported models might be unstable. For instance, based on a study of homogeneous spheroids, they suggest that nonrotating stellar systems with flattenings greater than  $\sim 1:3$  may be unstable to global bending modes. Little of the Soviet work has been verified by  $N$ -body studies of realistic models, however.

In the present paper, we investigate the stability of perhaps the simplest family of nonspherical models with realistic density profiles, the oblate “shell-orbit” models first described by Bishop (1987). Bishop models are constructed entirely out of short-axis tube orbits with zero radial thickness. The existence of these orbits, in particular oblate potentials, was demonstrated by Hori (1962), Meys (1981), and Richstone (1982). De Zeeuw (1985) showed that shell orbits are present at any energy in ellipsoidal Stäckel (1890) potentials, being just the limiting form of the “tube” orbits as the radial epicyclic motion vanishes. In spherical or disk models, shell orbits are exactly circular; in oblate models, they are inclined circles which precess slowly about the symmetry axis. Here we study the stability of shell-orbit models based on the Kuzmin-de Zeeuw oblate-spheroidal mass model

$$\rho(\tilde{m}) = \frac{\rho_0}{(1 + \tilde{m}^2)^2}, \quad \tilde{m}^2 = \frac{\varpi^2}{a^2} + \frac{z^2}{c^2}, \quad a > c, \quad (1)$$

for which the equations of motion are separable in prolate-spheroidal coordinates (Kuzmin 1956; de Zeeuw 1985). [Hereafter model flattenings will be given in Hubble's notation  $E_n$ , where  $n = 10(1 - c/a)$ .] A method for constructing shell-orbit solutions to this mass model has been outlined by Bishop (1987).

Because orbits in oblate potentials conserve one component of the angular momentum, shell-orbit models can be made to "rotate" by specifying that unequal fractions of stars travel clockwise and counterclockwise at any radius. In the present paper, and in future papers in this series, only completely nonrotating models will be considered. The primary justification for this restriction is that real elliptical galaxies, to the extent that they rotate, probably experience some degree of figure rotation (Binney 1987), and little progress has been made yet on analytic construction of models with rotating figures.

In § II we consider the axisymmetric stability of Bishop's models, first by presenting an approximate criterion for short-wavelength stability, and then by  $N$ -body integration. We find that models flatter than  $\sim E6$  are axisymmetrically unstable. In § III we present the results of three-dimensional  $N$ -body simulations, which reveal that shell-orbit models of *all* flattenings—even nearly spherical—are subject to a dipole, or " $m = 1$ ," instability that gradually increases the radial velocity dispersion of these models. Thus our results show that no radially "cold," oblate model can be stable, even in the absence of rotation. In § IV we discuss the possible relevance of these results to real elliptical galaxies.

Many  $N$ -body studies of rapidly rotating disks are based on models containing an inert "halo" component. All our calculations are based on self-contained models, without halos.

## II. AXISYMMETRIC STABILITY

A sufficiently cold *disk* is unstable to clumping on short radial length scales (Toomre 1964). The dispersion relation for tightly wound, axisymmetric ( $m = 0$ ) oscillations in a smooth flat disk is

$$\omega^2 = \kappa^2 - 2\pi G \Sigma k F_1(k\sigma/\kappa) \quad (2)$$

(Kalnajs 1965; Lin and Shu 1966), with  $\kappa$  the local epicyclic frequency,  $\Sigma$  the disk surface density,  $\sigma$  the radial velocity dispersion, and  $k = 2\pi/\lambda$  the radial wavenumber;  $\omega^2 < 0$  denotes instability. The function  $F_1 \leq 1$  is the standard "reduction factor" that describes the decreased response of the disk below that of a perfectly cold one. This  $m = 0$  instability is unaffected by the direction of rotation of the stars, and we expect that nonrotating shell-orbit models will be similarly unstable when their flattenings are sufficiently great. In disks with small but finite scale heights  $h$ , the dispersion relation (2) becomes

$$\omega^2 = \kappa^2 - 2\pi G \Sigma k F_1(k\sigma/\kappa) F_2(kh), \quad (3)$$

where  $\kappa$  and  $\sigma$  are now defined by their values in the equatorial plane, and  $F_2 \leq 1$  is a second reduction factor arising (in part) from the fact that the potential disturbance caused by a given perturbation in surface density is weaker in a spheroid than in a perfectly flat disk. Toomre (1964), Shu (1968), and Vandervoort (1970) have given approximate expressions for  $F_2$  in the limit that the disk scale height is small compared to the radial wavelength, i.e.,  $kh \ll 1$ .

It is not clear to what extent the existing treatments of nearly flat disks are useful in predicting the critical flattening at which Bishop models become axisymmetrically unstable. We never-

theless give, in Appendix A, the derivation of a heuristic reduction factor based on the assumption that the  $z$ -dependence of the perturbation is just proportional to the unperturbed density. That reduction factor—which is similar to the ones derived by Shu (1968) and Vandervoort (1970)—predicts in the limit of short-wavelength oscillations in a radially cold disk that

$$\omega^2 = \kappa^2 - 4\pi G \langle \rho(\varpi, z) \rangle_z, \quad (4)$$

where the angle brackets indicate a density-weighted average over  $z$ . For the Kuzmin-de Zeeuw oblate model, axisymmetric instability then requires

$$\kappa < 2.80 [G\rho(\varpi, 0)]^{1/2} \approx \omega_z, \quad (5)$$

where  $\omega_z$  is the  $z$ -oscillation frequency. Figure 1 shows the functions  $\kappa^2(\varpi, 0)$  and  $4\pi G \langle \rho(\varpi, z) \rangle_z$  for Kuzmin-de Zeeuw oblate spheroids of various flattenings. According to that figure, shell-orbit models flatter than  $\sim E7$  should be axisymmetrically unstable. However, this conclusion is very dependent on the precise value of the numerical coefficient in the dispersion relation (5); increasing or decreasing that coefficient by only 20% shifts the stability boundary from  $E6.5$  to  $E8$ . We conclude that the critical flattening for axisymmetric stability of radially cold, oblate models is probably difficult to compute with any accuracy from simple linear theory.  $N$ -body simula-

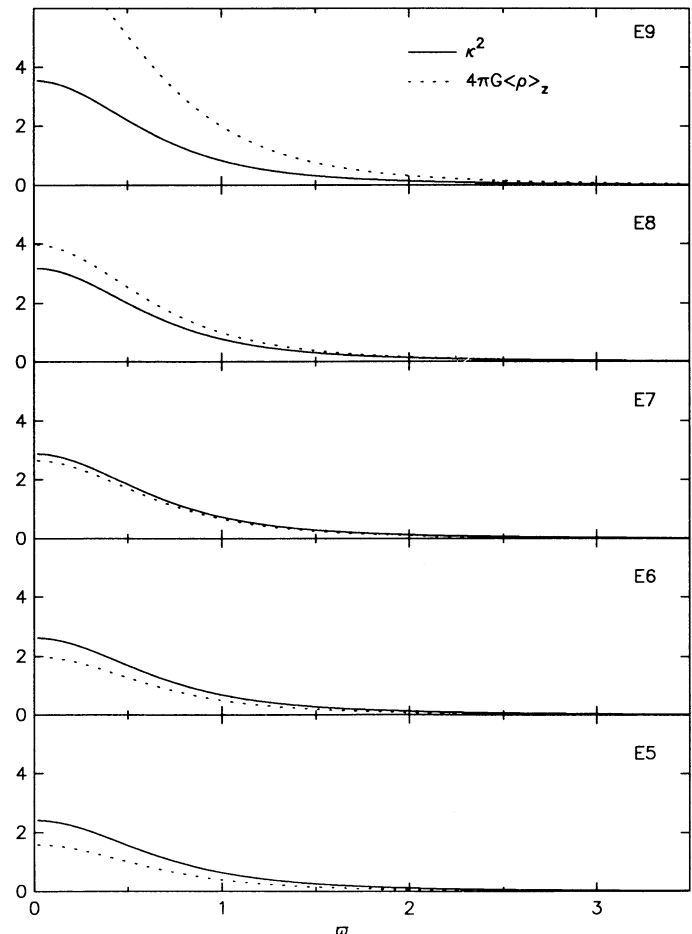


FIG. 1.—Epicyclic and mean  $z$ -oscillation frequencies as a function of equatorial radius in Kuzmin-de Zeeuw oblate mass models of various flattenings.

tions are therefore an indispensable guide. Nevertheless, the analysis in Appendix A does make one prediction that is likely to be qualitatively correct: unlike the case of an indefinitely thin disk, the growth rate  $\omega$  in a cold oblate model remains finite as the wavelength is decreased. This means that  $N$ -body simulations are likely to give qualitatively correct results even though limited in spatial and temporal resolution.

Axisymmetric stability of a set of shell-orbit models was tested by evolving 20,000 particle realizations of Bishop's models with an  $N$ -body code that enforces axial symmetry. The algorithm for generating initial coordinates and velocities is described in Appendix B. Since the Kuzmin-de Zeeuw oblate spheroid is infinite in extent, initial realizations were generated from models truncated on oblate surfaces such that

$$\omega^2 + \left(\frac{a}{c}\right)^2 z^2 = 10^2, \quad (6)$$

corresponding to  $\sim 5$  half-mass radii. Truncation on an iso-density surface leaves the interior force field unchanged. Self-consistent orbital distributions were then derived using Bishop's (1987) prescription, modified to include only orbits with turning points inside of the truncation surface. The resulting models are finite in extent and precisely in equilibrium. Although a sharp truncation may seem dangerous from the point of view of stability, the density of particles at our truncation surface is so low ( $\sim 10^{-4}$  times the central space density;  $\sim 10^{-3}$  times the central surface density) that we do not expect the overall evolution to be noticeably affected. It is common practice in disk simulations to truncate models much farther in (e.g., Zang and Hohl 1978).

The axisymmetric  $N$ -body code is similar to the one described by van Albada and van Gorkom (1977) is that the gravitational potential is evaluated through an expansion in spherical harmonics at each radius, assuming no dependence of the density on azimuthal angle  $\phi$ :

$$\Phi(r, \theta) = -Gm \sum_{l=0}^N P_l(\cos \theta) A_l(r), \quad (7a)$$

$$A_l(r) = r^{-(l+1)} \sum_{r' < r} r'^l P_l(\cos \theta') + r^l \sum_{r' > r} r'^{-(l+1)} P_l(\cos \theta'), \quad (7b)$$

with  $P_l(\cos \theta)$  a Legendre polynomial,  $\cos \theta = z/r$ ,  $m$  the mass of an individual particle,  $G$  Newton's constant, and  $N = 6$  in the present case. The summations are over particles interior or exterior to the radius  $r$ . The radial functions  $A_l(r)$  were evaluated at each time step on a uniform radial grid of 100 steps, and intermediate values were interpolated. Inclusion of terms up to  $l = 6$  was found sufficient to evaluate the potentials of models as flat as  $\sim E8$  without significant loss of accuracy. Finally, the innermost 5% of the particles were fixed throughout the integration, to avoid problems with inaccurate potential expansions at radii containing only a small number of particles. Hereafter, all quantities are expressed in units such that  $G = M = a = 1$ , with  $M$  the mass of the *untruncated* model. The period of a circular orbit at the half-mass radius of the spherical model is 30.3 in these units; a circular orbit at the center of the E8 model has period 7.05. The integration time step was 0.02.

Figure 2a illustrates the axisymmetric evolution of the E8 model. The central regions of the model laminate into thin, curved cylinders on a time scale that is of order the orbital period in the core; the amplitude of the density increase is roughly constant with height  $z$ . Not surprisingly, as Figure 2b

shows, the loci of enhanced density lie nearly along the prolate-spheroidal coordinate surfaces that define the unperturbed orbital motion. What is more surprising is that these condensations, once formed, *persist* without much change until the end of the integration at  $t = 100$ . Toomre (1964) and Shu (1969), for instance, guessed that condensations like those in Figure 2 would rapidly dissipate due to random motions generated during their formation. Evidently this is not the case, at least when the potential is forced to remain precisely axisymmetric. A plot of the final radial density profile of the E8 model (Fig. 3) shows that all the condensations are close to one grid cell in width, consistent with the expectation that the shortest radial wavelengths are the most unstable. The model is clearly unstable at all radii  $\varpi \leq 5$  and shows hints of evolution at larger radii.

The most important question to be answered by the  $N$ -body integrations is the critical model flattening at which axisymmetric instability is suppressed. We quickly discovered that this question is difficult to answer with any certainty, since perfectly cold models, even if (locally) stable, are responsive to collective effects which amplify any perturbations and lead to large transient enhancements in the local density. To reduce these transient effects, we computed, in each radial grid cell, the *time-averaged* overdensity; for truly stable models, this average should tend to zero after several orbital periods. Figure 4 shows the dependence on time of the quantity

$$\left[ \frac{1}{100} \sum_{i=1}^{100} \left( \frac{\langle m_i - m_{i,0} \rangle}{m_{i,0}} \right)^2 \right]^{1/2}, \quad (8)$$

where  $m_i$  is the mass in grid cell  $i$ ,  $m_{i,0}$  is the initial mass in the cell, and the angle brackets indicate a time average from  $t = 0$  to the current time. Figure 4 suggests that models as flat as, or flatter than, E6 are axisymmetrically unstable; the amount of evolution does not appear to change as the flattening is reduced from E5 to E4. A plot of the actual time dependence of the density in the innermost grid cells likewise suggests that the stability boundary lies near E6. Although rounder models may be axisymmetrically unstable at some level, Figures 3 and 4 suggest that the nonlinear evolution of these models is so small as to be physically unimportant.

The axisymmetric instability described here was apparently also seen in  $N$ -body simulations of radially cold, oblate models by de Zeeuw *et al.* (1983), Bishop, Duncan, and Lee (1987, reported in Bishop 1988), and Shapiro and Teukolsky (1987). The first set of authors analyzed a family of E5.8 models using an axisymmetric code and reported a ring instability in the coldest models. The second group of authors found (using as few as 1000 particles) that an E8 shell-orbit model was ring-unstable, while an E6 model appeared stable. The final set of authors saw an axisymmetric instability in homogeneous oblate models flatter than about E6, using a general relativistic code specialized to the Newtonian limit.

### III. THREE-DIMENSIONAL STABILITY

#### a) Expectations

Relatively little is known about the nonaxisymmetric or global stability of radially cold, nonrotating stellar systems. Work published to date suggests that, while a radially cold *disk* is likely to be unstable to a variety of modes, both axisymmetric and nonaxisymmetric, a radially cold *sphere* is stable.

Spherical systems composed of circular orbits are stable to perturbations that preserve the spherical symmetry

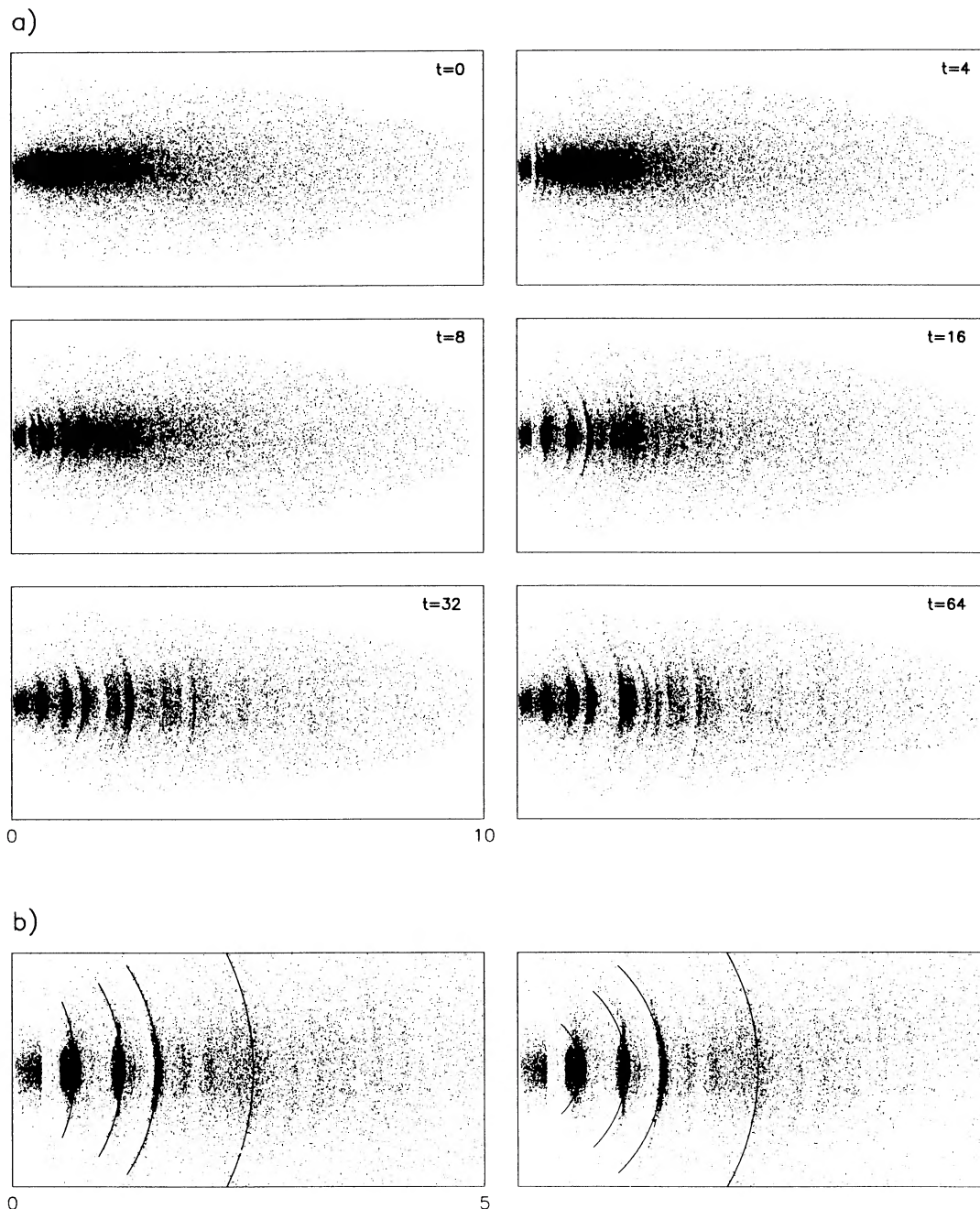


FIG. 2.—(a) Six snapshots of the E8 Bishop model, evolved with the axisymmetric  $N$ -body code ( $N = 20,000$ ). Particles are plotted in the  $(\varpi, z)$  plane. (b) The model at  $t = 16$ . The left frame shows curves of constant  $\lambda$ , along which shell orbits lie at  $t = 0$ ; the right frame shows circular curves with the same equatorial radii.

(Bisnovatyi-Kogan, Zel'dovich, and Fridman 1968). Stability to general perturbations has been demonstrated for spherical shell-orbit models with  $r^{-2}$  density laws by Synakh, Fridman, and Shukhman (1972), and for homogeneous models by Mikhailovskii, Fridman, and Epelbaum (1971) and Shukhman (1973). (However, Bisnovatyi-Kogan [1971] points out that the homogeneous model is susceptible to *linearly* growing dipole modes.) Recent  $N$ -body work, reported by various authors (e.g., Barnes, Goodman, and Hut 1986; Dejonghe and Merritt 1988) has revealed no convincing indication of instability in spherical shell-orbit models with realistic (flat or declining) density profiles.

The situation is very different for nonrotating disks. Reversing half the stars in a cold disk should greatly reduce the strength of at least the classic bar mode (Kalnajs 1977), but other modes may remain unstable. The only exact study of the global stability of a nonrotating stellar disk is that of Araki (1987), who analyzed the spectrum of normal modes of Kalnajs's (1972) simple family of disk models when half the stars are counterrotating. Kalnajs disks have a surface density equal to that of highly flattened, homogeneous oblate spheroids,  $\Sigma(r) \propto (1 - r^2/R^2)^{1/2}$ ,  $r \leq R$ . (Kalnajs's analysis, as well as Araki's, was limited to perturbations in the plane of the disk.) Araki found that most of the unstable modes of the rotating

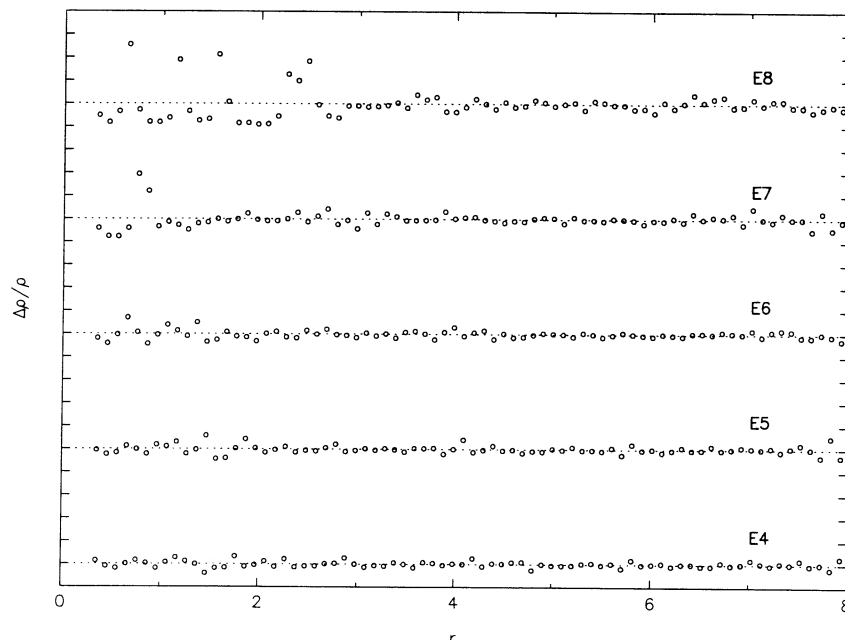


FIG. 3.—Radial density profile at  $t = 100$  for axisymmetrically evolved Bishop models. Plotted, at each radial grid point, is the fractional change in the mass of the spherical cell since  $t = 0$ . Tick marks on the vertical axes are separated by 1.

disks are stabilized in the counterrotating disks. However, sufficiently *cold* counterrotating disks—which are perhaps similar in their stability properties to highly flattened, shell-orbit models of the sort considered here—are unstable to a variety of modes. The simplest of these are the axisymmetric, or  $m = 0$ , modes discussed above and which are unaffected by reversal of half the stars. However, the most persistent mode is the  $(n, m) = (3, 1)$  mode, which is unstable in the counterrotating

disks as long as the rms azimuthal velocity exceeds 2.1 times the rms radial velocity. This mode produces a change in surface density equivalent to that produced by a rearrangement of disk matter according to the rule

$$r \rightarrow [1 + \epsilon(t)xr]r, \quad (9)$$

i.e., the density center of the disk moves away from the center of mass. The  $(3, 1)$  mode (like the other  $m = 1$  modes) has zero

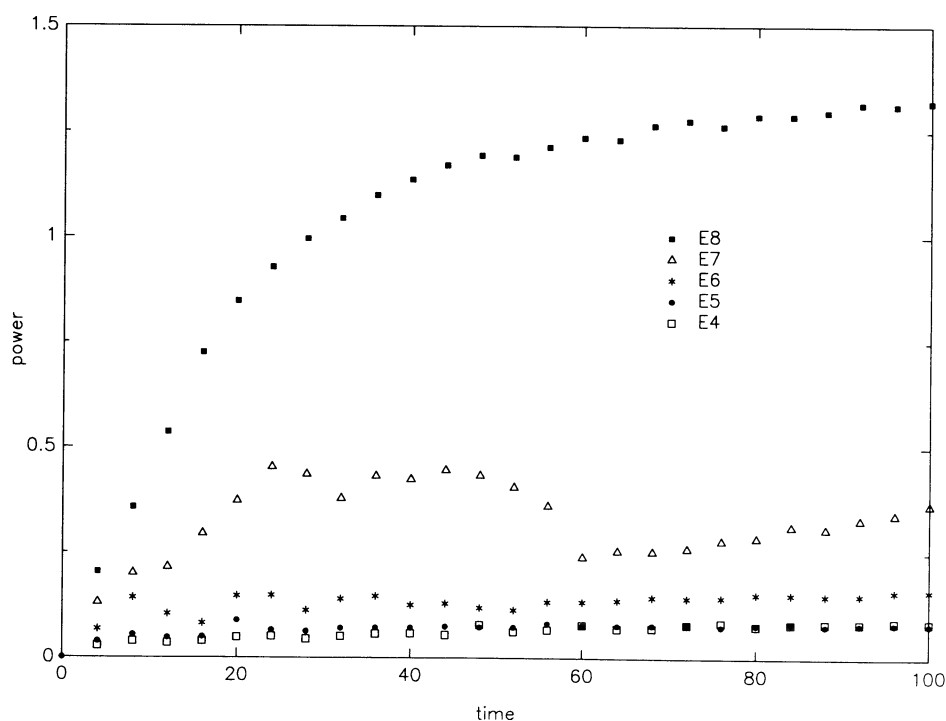


FIG. 4.—Time development of the time-averaged, rms overdensity in axisymmetrically evolved Bishop models (see eq. [8])

pattern speed and a growth rate that reaches a maximum of 0.92 times the (constant) disk angular speed in a perfectly cold model. Araki argues that, at its onset, the (3, 1) instability has a sort of “two-stream” character, since a model with the same orbital distribution but all stars orbiting in the *same* direction is stable to this mode. However even the *rotating* models become (3, 1) unstable when the orbits are made slightly more circular, and on this basis, Araki concludes that the instability is not fundamentally “two-stream” in character.

Although Araki’s results apply strictly only to the Kalnajs disks, there is some evidence that  $m = 1$  modes may be the dominant ones in more realistic, slowly rotating disk models. For instance, Zang and Hohl (1978) find increasingly prominent one-armed features, and increasingly weak bars, in  $N$ -body simulations of two families of disk models as the percentage of retrograde stars is increased, and they cite some linear theory calculations of a third family of models which predict similar behavior. Araki also argues via the WKB formalism that  $m = 1$  modes are the only ones (aside from  $m = 0$ ) that are likely to be unstable, with zero pattern speed, in general disk models. Based on this work, we might expect that Bishop models—although probably stable in the spherical limit—become unstable to global,  $m = 1$  modes as their flattening is increased.

Finally we note that Bishop, Duncan, and Lee (1987, reported in Bishop 1988) carried out full  $N$ -body integrations of essentially the same models studied here and noticed no non-axisymmetric instabilities. Their integrations were based on only 1000 or 2000 particles, and this fact may explain why they failed to notice the instability that we report below.

### b) Integration

The general stability of the shell-orbit models was tested by evolving 20,000 particle realizations in a code that retained nonaxisymmetric as well as axisymmetric terms in the potential expansion at each radius:

$$\Phi(r, \theta, \phi) = -Gm \sum_{l=0}^6 \sum_{m=0}^l P_l^m(\cos \theta) \times [A_l^m(r) \cos(m\phi) + B_l^m(r) \sin(m\phi)], \quad (10a)$$

$$A_l^m(r) = \epsilon_m \frac{(l-m)!}{(l+m)!} \times \left[ r^{-(l+1)} \sum_{<r} r'^l P_l^m(\cos \theta') \cos(m\phi') + r^l \sum_{>r} r'^{-(l+1)} P_l^m(\cos \theta') \cos(m\phi') \right], \quad (10b)$$

$$B_l^m(r) = \epsilon_m \frac{(l-m)!}{(l+m)!} \times \left[ r^{-(l+1)} \sum_{<r} r'^l P_l^m(\cos \theta') \sin(m\phi') + r^l \sum_{>r} r'^{-(l+1)} P_l^m(\cos \theta') \sin(m\phi') \right], \quad (10c)$$

where  $\epsilon_0 = 1$ ,  $\epsilon_m = 2$  ( $m = 1, 2, 3, \dots$ ). This code is a version of the one described originally by T. S. van Albada (1982) and improved by later workers (Bontekoe 1988; Bertin and Stiavelli 1989). It differs in implementation from the axisymmetric code described above in two important respects. First, the

three-dimensional code evaluates all quantities associated with the potential on an *angular* as well as a radial grid, in spite of the fact that the angular dependences are given explicitly and simply by the expression (15a). The use of an angular grid increases the computational speed. Second, the center about which the potential expansion was computed (hereafter referred to as the “grid center”) in the three-dimensional code was shifted every 20 time steps in such a way as to follow the movement of the density center, and no particles were “frozen.” The precise centering algorithm is discussed below. All the three-dimensional simulations were based on a grid with 50 radial steps, spaced quadratically, 12 steps in  $\theta$ , and 24 steps in  $\phi$ . The time step was 0.01 in the units defined above. Modest changes in the time step and the radial grid spacing were found not to affect the evolution appreciably. Complete runs (until  $t = 320$ , or roughly 10 full periods of a circular orbit at the half-mass radius) required about 90 hours on a Vax 3500 computer.

### i) Density Evolution

Figure 5a shows the three-dimensional evolution of the E8 shell-orbit model. (Only 4000 of the 20,000 particles are displayed.) The snapshots in Figure 5a show the model, projected along the initial symmetry axis, at times 0, 5, 10, 20, 40,  $\dots$ , 320. The most striking feature at early times ( $t \approx 10$ ) is the formation of a sharp circular ring at radius  $r \approx 0.5$ , presumably through the same axisymmetric mechanism discussed above. Note however that the core (which was not frozen in these runs) is completely evacuated during the formation of the ring. Between  $t = 10$  and  $t = 20$ , the ring collapses, non-axisymmetrically, into a very tight nucleus which persists until the end of the simulation. Immediately after its formation ( $t = 20$ ), the new core lies noticeably away from the original density center. After  $t = 20$ , the model continues to form sharp, essentially circular rings at larger and larger radii; however, the bulk of the matter within the largest ring is always clearly *displaced* from the original density center. This displacement occurs roughly along a fixed axis. By  $t = 320$ , the ring formation has apparently stopped, and the model appears to be approaching an equilibrium, roughly axisymmetric state.

Clearly the three-dimensional evolution of the E8 model differs strongly from the axisymmetric, fixed-center evolution shown in Figure 2. The most important difference is the slow growth of a lopsided, essentially dipole “mode” that first becomes noticeable after the formation and collapse of the central ring at  $t \approx 10$ . We were initially skeptical of the reality of this nonaxisymmetric evolution. The harmonic expansion code (like virtually every  $N$ -body code that does not compute forces from a direct pairwise summation) does not conserve total linear momentum, whether or not the grid center is allowed to move. In earlier runs (not shown here), we used a centering algorithm that placed the origin of the grid at the center of mass of the roughly 500 most bound particles. This algorithm performed poorly after the formation of the central ring: because there was no well-defined density center, the grid tended to wander erratically, leading to large shifts in the model’s center of mass. We therefore worried that the slow growth of the nonaxisymmetric deformation—which only appears *after* the evacuation of the core—might be a spurious effect. After some experimentation, we adopted a centering algorithm (used subsequently in all the  $N$ -body integrations with this code) that simply followed the center of mass of all particles within a radius 1 from the previous grid center, a

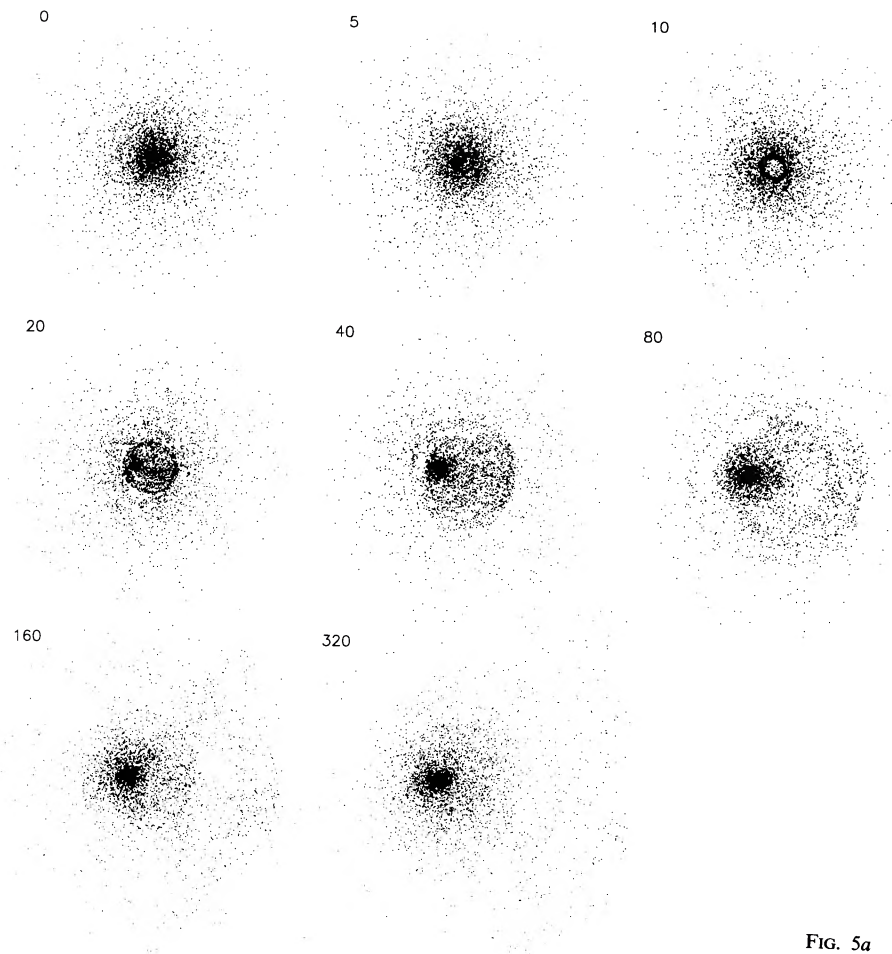


FIG. 5a

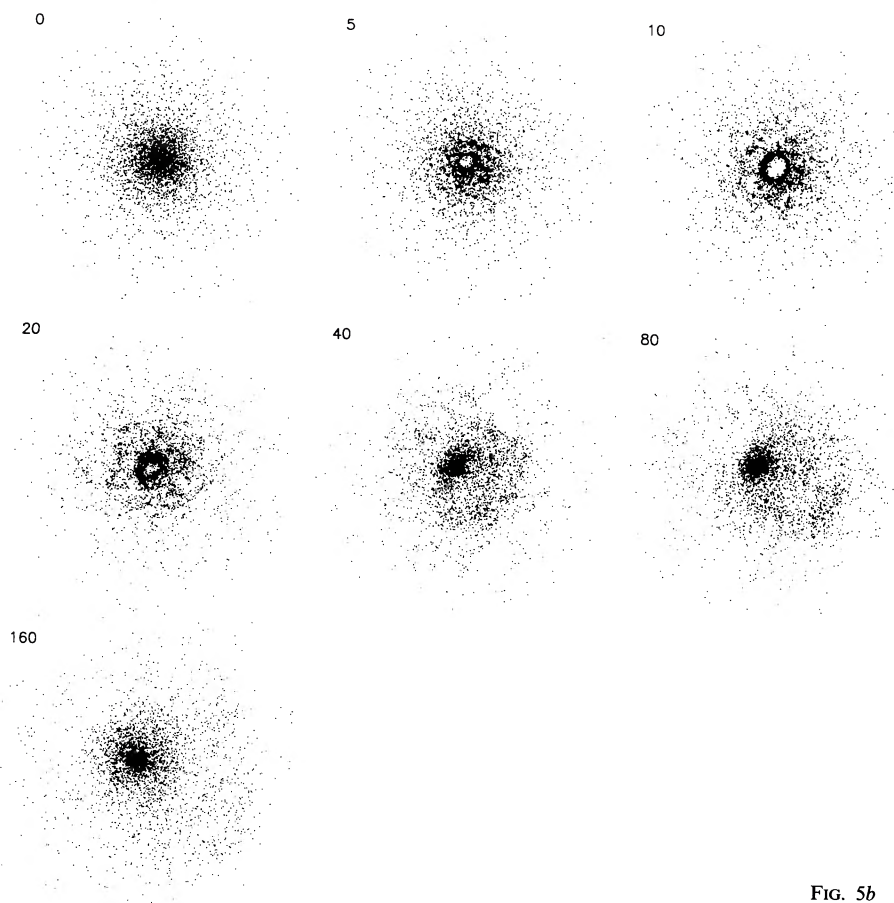


FIG. 5b

FIG. 5.—Snapshots of the E8 Bishop model, evolved with the three-dimensional  $N$ -body codes. Each picture is a projection parallel to the  $z$ -axis. (a) Harmonic-expansion code;  $N = 20,000$ ; 4000 points plotted. (b) Tree code;  $N = 4000$ .

radius sufficiently large to contain the entire central ring. Both algorithms produced qualitatively similar results, but the latter resulted in center-of-mass displacements of only  $\sim 1$  for the E8 model. (By contrast, a run with *fixed* grid center produced a runaway of the center of mass.)

Although small, these center-of-mass displacements were still large enough to cast doubt in our minds on the reality of the slowly growing, nonaxisymmetric evolution found with the three-dimensional code. We therefore decided to carry out a second integration of the E8 model using a code with a potential solver that is not dependent for its accuracy on a “correct” choice of the density center. Lars Hernquist kindly provided us with a copy of his “tree” code, a modified direct-summation  $N$ -body code in which forces from distant groups of particles are approximated by a single contribution from their center of mass (see Hernquist 1987). The tree code contains only three important adjustable parameters: the time step, set to the same value, 0.01, as in the harmonic-expansion code; the particle softening length, set to 0.2; and the accuracy parameter  $\theta$  that determines the angular size of groups of particles whose internal structure is ignored, set to 0.8 rad. Figure 5b shows the tree-code integration, until  $t = 160$ , of a 4000 particle realization of the E8 model. (This run required  $\sim 900$  hours of CPU time on a Sun 4/260 computer.) The agreement with the earlier integration is very good: both runs produce a central ring at  $t \approx 10$ , followed by formation of an off-center compact core and the slow growth of a lopsided deformation. The most obvious difference between the two integrations is the appearance of small-angular scale features in the tree-code simulation at early times (Fig. 5b,  $t = 10, 20$ ). These features are no doubt “real”; they are precluded in the 20,000 particle integration by the limited angular resolution of the potential expansion. By contrast, the harmonic-expansion code permits the formation of very sharp *radial* features at small radii (Fig. 5a,  $t = 20, 40$ ) which are not seen in the tree-code integration because of the

relatively large softening length. In short, although there are differences in the abilities of the two codes to handle small-scale features, both predict essentially identical, large-scale evolution of the model.

The two simulations shown in Figures 5a and 5b were based on different numbers of particles and therefore began from slightly different random realizations of the same model. As a further check on the global evolution, we used the harmonic-expansion code to integrate the *same* 4000 particle realization of the E8 model integrated by the tree code. Again the evolution was very similar; but in addition, the azimuthal *orientation* of the slowly growing deformation was nearly the same in the two runs, differing by at most  $10^\circ$ . This agreement confirms even more strongly that the instability is inherent in the model and not simply a spurious product of the  $N$ -body codes.

A further comparison between the two 4000 particle integrations of the E8 model is made in Figure 6, which shows the amplitudes, at  $t = 80$ , of the various angular components of the potential expansion. Plotted are the quantities

$$\log_{10} \frac{[\sum (|A_l^m|^2 + |B_l^m|^2)]_{t=80} / |A_0^0|^2}{[\sum (|A_l^m|^2 + |B_l^m|^2)]_{t=0} / |A_0^0|^2}, \quad (11)$$

where the coefficients were computed with respect to the center of mass (not the grid center); the sum is over radial grid steps, without any additional weighting by mass or density. Figure 6 shows that the model at  $t = 80$  has developed substantial power in two sorts of angular harmonics. The “odd-odd” harmonics, e.g.,  $(l, m) = (1, 1), (3, 1), (3, 3)$ , imply a mass distribution that is symmetric about the equatorial plane, but with a shift of the density center away from the center of mass (see Bontekoe 1988 for a graphical depiction of the spherical harmonic weighting functions). The “even-even” harmonics, e.g.,  $(l, m) = (2, 2), (4, 2), (4, 4)$ , correspond to barlike deformations parallel to the equatorial plane. Even-odd or odd-even

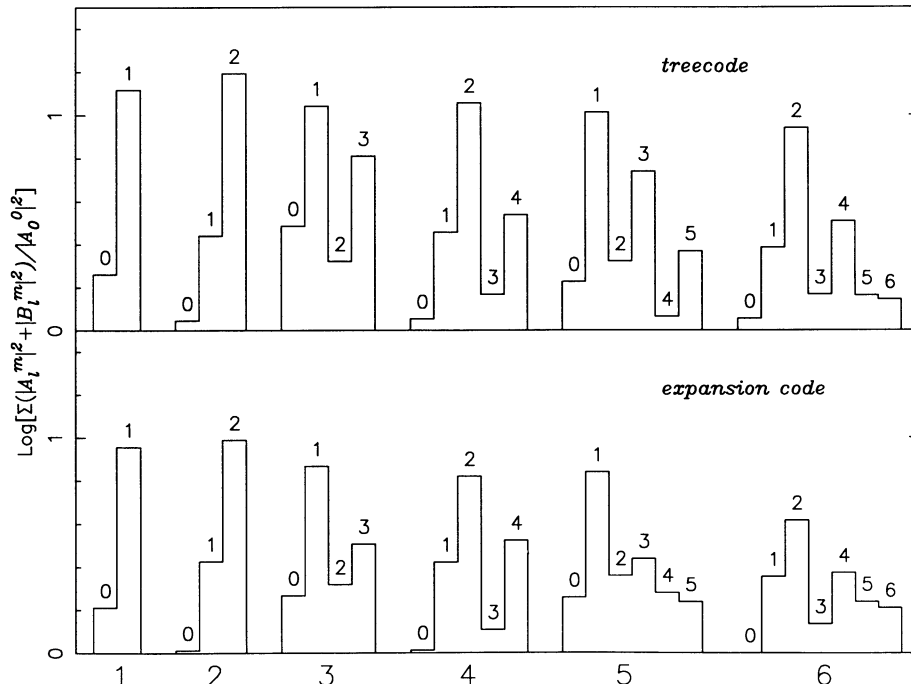


FIG. 6.—Angular components  $(l, m)$  of the potential expansion of the E8 models at  $t = 80$ , computed from the two runs with  $N = 4000$  (see eq. [11])

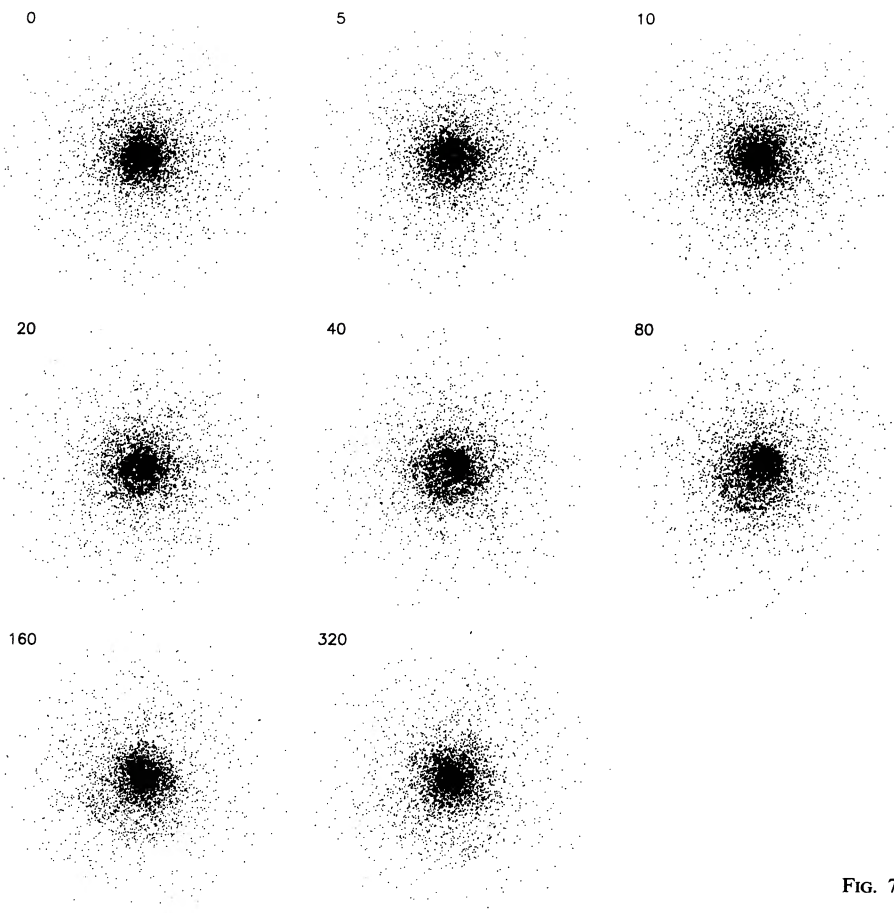


FIG. 7a

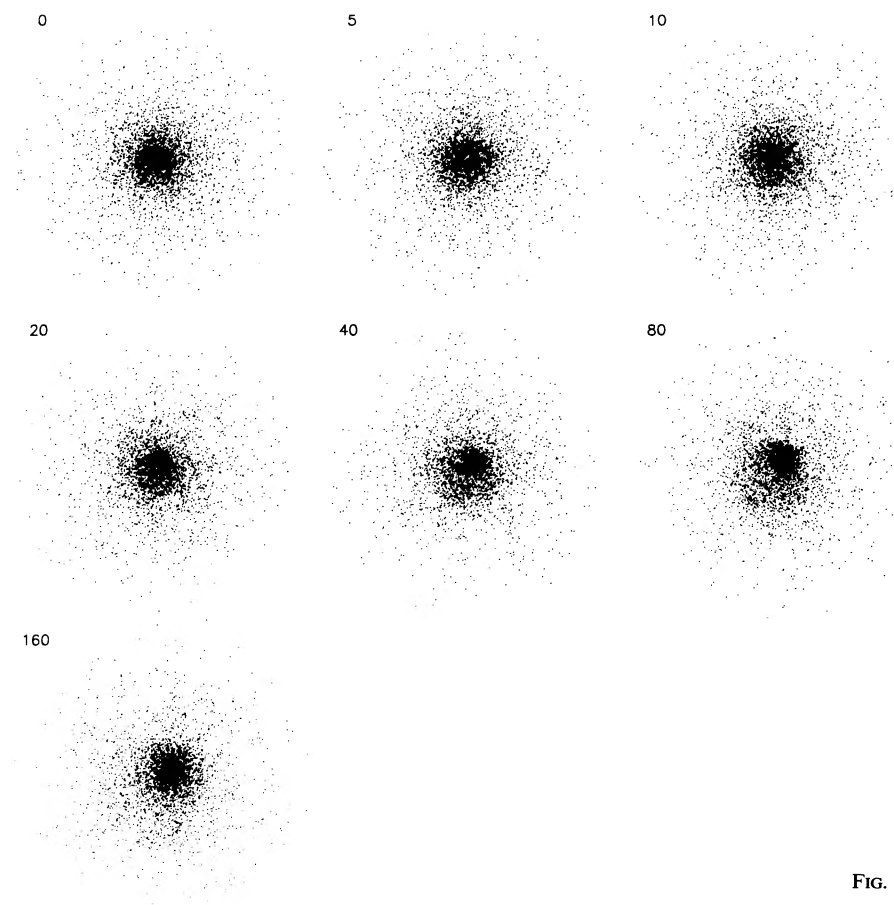


FIG. 7b

FIG. 7.—Snapshots of the E3 Bishop model, evolved with the three-dimensional  $N$ -body codes. Each picture is a projection parallel to the  $z$ -axis. (a) Harmonic-expansion code;  $N = 4000$ . (b) Tree code;  $N = 4000$ .

harmonics—describing deformations that are *not* symmetric with respect to the equatorial plane, i.e., bending modes—remain small. These plots indicate that the E8 model evolves strongly on a variety of angular scales, including the smallest angular scales resolvable with the harmonic expansion code, and that the dominant evolution is symmetric about the equatorial plane. In this sense, the model behaves in a manner very similar to that of the coldest nonrotating disk models analyzed by Araki (1987) (although our model at  $t = 80$  has clearly evolved out of the linear regime).

Once convinced of the reality of the nonaxisymmetric evolution seen in the E8 model, we carried out a set of integrations of the E3 model. As Figures 7*a* and 7*b* show, the latter model exhibits no tendency toward axisymmetric ring formation, consistent with the result described above that models rounder than  $\sim$ E6 are axisymmetrically stable. Nevertheless, there is a slow and very clear movement of the core away from its original location in both integrations. Figure 8 shows the amplitudes of the various angular harmonics for the 4000 particle E3 integrations at  $t = 80$ , again compared to the values at  $t = 0$ . The (1, 0) harmonic appears large on these plots only because of a particularly small initial amplitude; otherwise, only the (1, 1) dipole and (2, 2) bar terms show significant growth. The model flattening (as reflected in the axisymmetric coefficients) does not change appreciably, which suggests that the instability moves particles roughly parallel to their orbital planes, without strongly affecting the orbital inclinations.

Finally, we carried out a set of 20,000 particle integrations of a set of models with initial flattenings E7, E6, E5, E4, E2, and E1 using only the harmonic-expansion code. All these models showed significant nonaxisymmetric evolution; the dominant character of this evolution was always a gradual movement of the density center away from the center of mass. That the instability is present even in models that are nearly round is demonstrated in Figure 9, which shows the E1 model at  $t = 40$

in two projections designed to enhance detail. The dipole deformation is very clear; it is also very simple, in that it shows little dependence on  $z$ . Figure 10 shows the evolution of the amplitude of the dipole contribution to the potential, computed with respect to the center of mass, in each of the 20,000 particle integrations. The quantity plotted is  $(|A_1^1|^2 + |B_1^1|^2)^{1/2}/|A_0^0|$ , where the coefficients were evaluated at  $r = 2$ , and only the contributions from interior particles were included (see [10]). Note that these coefficients are simply

$$A_1^{1(\text{int})}(r) \propto r^{-2} \int \rho x d^3x, \quad B_1^{1(\text{int})}(r) \propto r^{-2} \int \rho y d^3x, \quad (12)$$

where the integrals extend over the entire model interior to  $r$ . Judging from Figure 10, there is a fairly steady decrease in the strength of the evolution as the initial models are made rounder. At early times ( $t \lesssim 40$ ), there is a clear separation in this plot between the E7 and E8 models, which are strongly axisymmetrically unstable, and the rounder models. It seems likely that the early growth of the  $m = 1$  deformations in the E7 and E8 models is strongly affected by the (rapidly nonlinear) formation of rings in these models.

It would clearly be of interest to demonstrate rigorously that the nonaxisymmetric evolution found here is a true mode, and to calculate its functional form and growth rate in the linear regime for each of the models. We consider these questions to be beyond the scope of the present paper. Here we simply show, in Figure 11, the evolution of the radial dependence of the  $A_1^1(r)$  dipole term (calculated with respect to the center of mass) at early times for the three roundest models. In each case, the radial shape of the dipole term remains approximately fixed as it grows. The growth rate at early times ( $t \approx 5$ ) appears to be of order 0.1 for these models and to decrease with increasing model roundness; however, these models appear to be already in the nonlinear regime by  $t = 5$ . An E0

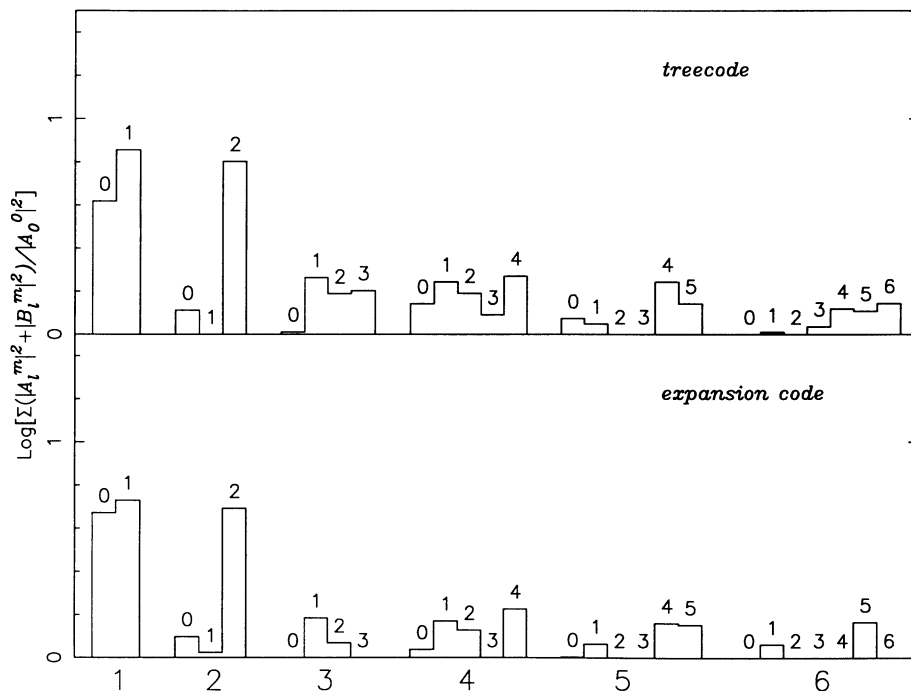


FIG. 8.—Same as Fig. 6, for the two E3, 4000 particle integrations

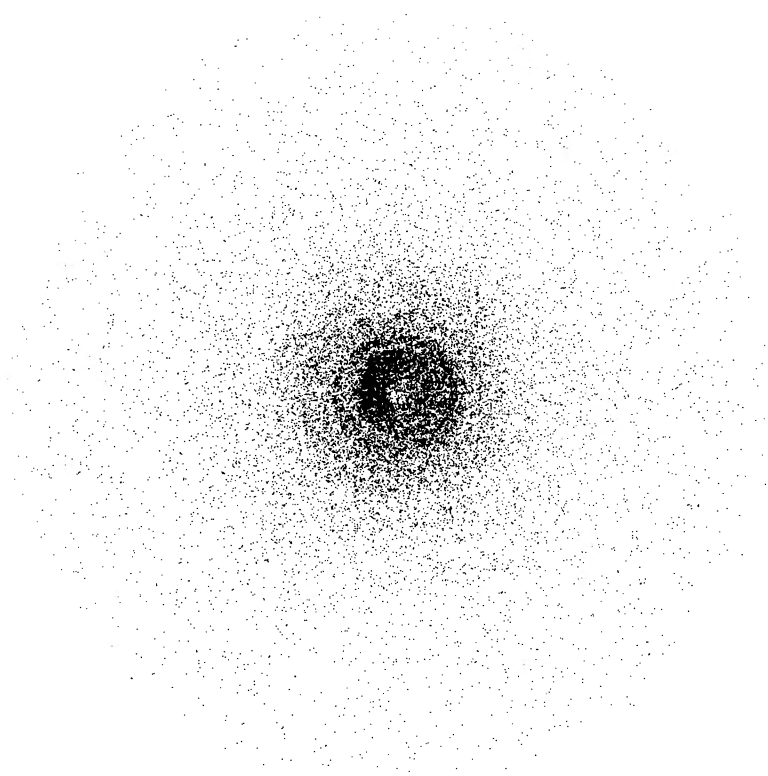


FIG. 9a

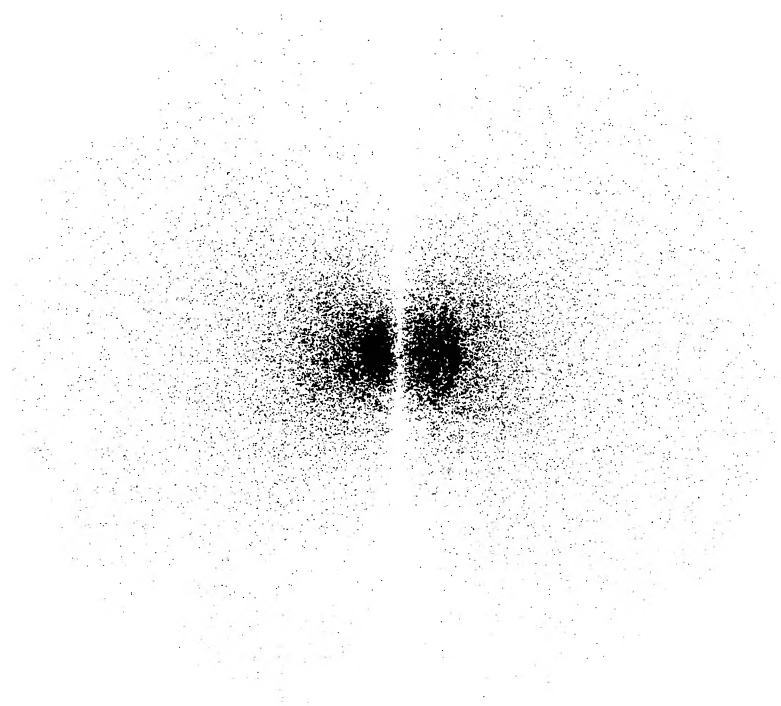


FIG. 9b

FIG. 9.—Snapshot of the E1 Bishop model at  $t = 40$ , as evolved with the harmonic-expansion code ( $N = 20,000$ ). (a) Particles have been rotated onto the equatorial plane with fixed  $r^2 = w^2 + z^2$ ; thus a spherical shell appears as a ring. (b) Particles have been rotated onto the  $y = 0$  plane with fixed  $w^2$ .

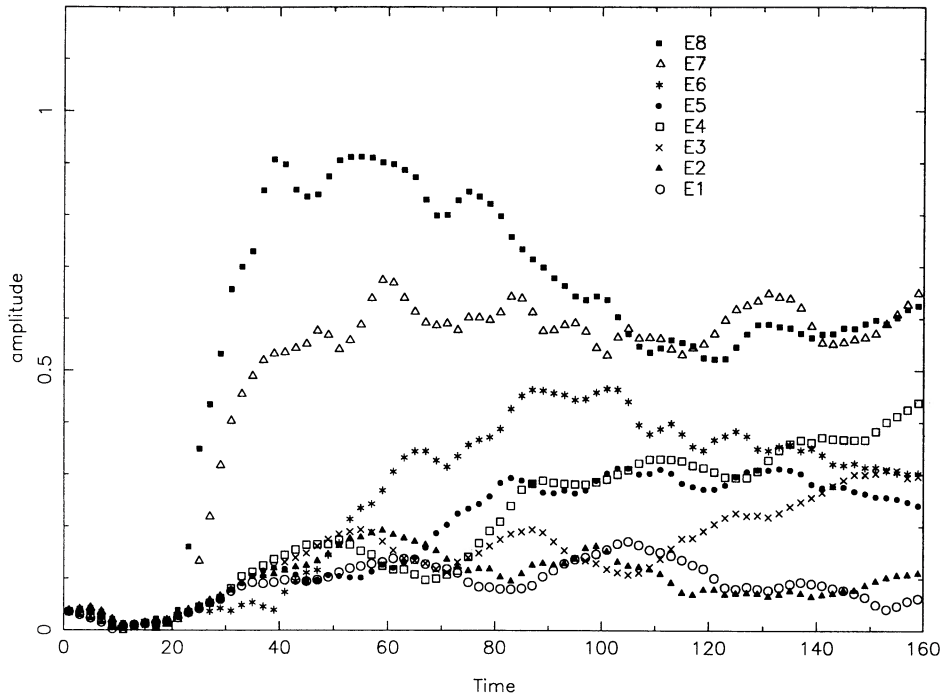


FIG. 10.—Time development of the amplitude of the dipole contribution to the potential in each of the 20,000 particle integrations (see eq. [12])

(spherical) model, which we also evolved, showed no sign of unstable evolution in any of the potential terms, suggesting that the growth rate of the dipole “mode” goes to zero for a

perfectly round model. This result is consistent with the earlier work on global stability of spherical stellar systems summarized above.

We consider next how the overall mass distribution of the Bishop models is affected by the instability. Figure 12 shows initial and final density profiles, as seen from the  $z$ -axis, for the E8 and E3 models. The E3 model has hardly evolved in this plot; however, the E8 model shows a much higher central density and a more extended envelope. Both features are natural end-products of gravitational torques resulting from the nonaxisymmetric instability. However, the high central density is probably more a result of the formation and collapse of a central ring at  $t \approx 10$  in this model. Note the “knee” at  $R \approx 5$ : in a plot of the projected density at  $t = 440$ , this knee has moved outward, suggesting that it is a signature of incomplete relaxation. The change in flattening of these models is shown in Figure 13. Again, the E3 model appears nearly unchanged, but the E8 model has clearly become *rounder*, at least near the center, as a result of the instability. Measurement of the isophotal contours gives approximate flattenings of E0 ( $\varpi \lesssim 0.5$ ), E5 ( $\varpi \approx 1$ ), and E7 ( $\varpi \approx 4$ ) at  $t = 320$ . At larger radii, the model is clearly not relaxed. Nevertheless, it is intriguing that, within the nearly relaxed region, the (initially) E8 model is never flatter than observed ellipticals (E0–E7). This result provides a certain amount of support for the hypothesis of Fridman and Polyachenko (1984, Vol. 2, p. 159) that dynamical instabilities are responsible for setting a limit to the flattening of real elliptical galaxies. However, the mechanism that they invoke for enforcing the limit—namely, a buckling or “firehose” instability—does not appear to be active in these models.

#### ii) Kinematic Evolution

One product of the development of nonaxisymmetric instabilities in the Bishop models is a gradual increase of radial kinetic energy. Figure 14 shows the evolution with time of the

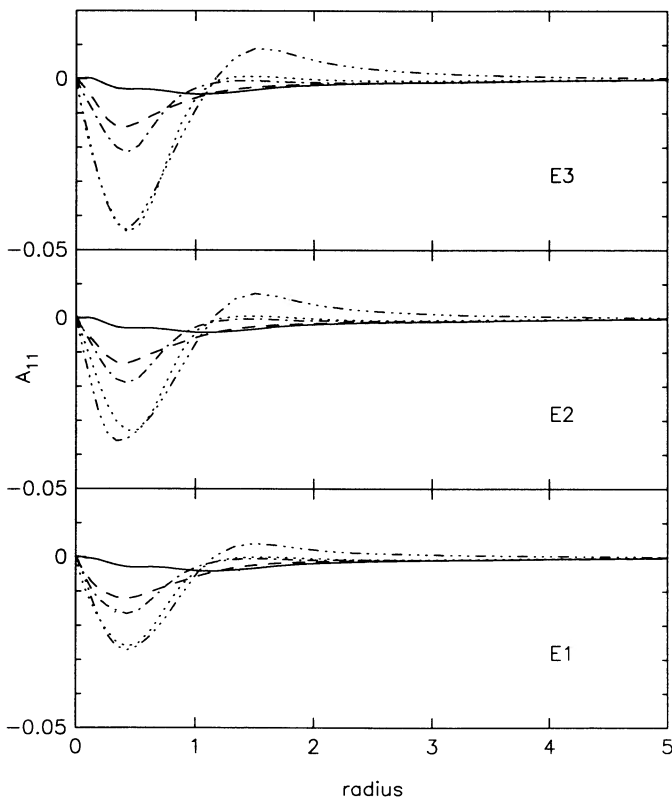


FIG. 11.—Evolution of  $A_1^1(r)$  for the three roundest models. Curves are shown at times  $t = 0, 5, 10, 20, 40$ .

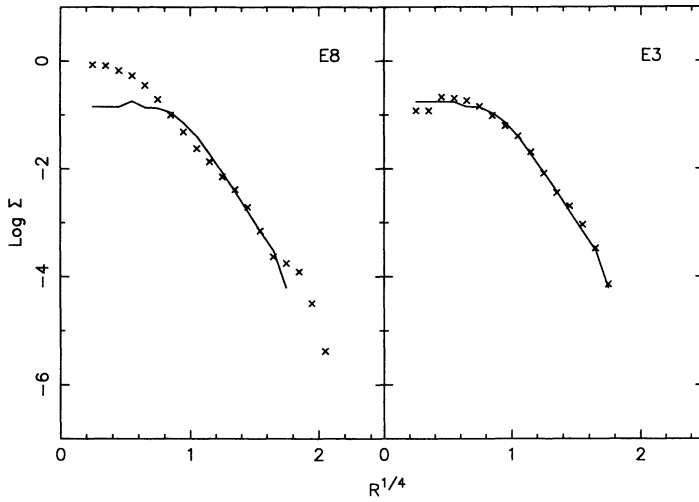


FIG. 12.—Surface density profiles, projected parallel to the  $z$ -axis, for the E8 and E3 models at initial (lines) and final (crosses) time steps

quantity  $2T_r/(2T_r + T_t)$  for each of the models, where  $T_r$  is the total kinetic energy in radial motions and  $T_t$  is the tangential kinetic energy, including both  $\theta$  and  $\phi$  components. This parameter varies from (approximately) zero in the initial models to  $\frac{1}{2}$  for an isotropic sphere and  $\frac{2}{3}$  for an isotropic disk (i.e., a disk in which the velocity dispersion is independent of direction in the disk plane). All the models appear to be still evolving slowly at the final time step; nevertheless, it is obvious that by  $t = 320$ , the various instabilities have acted to greatly increase the radial kinetic energy in the flatter models. Very

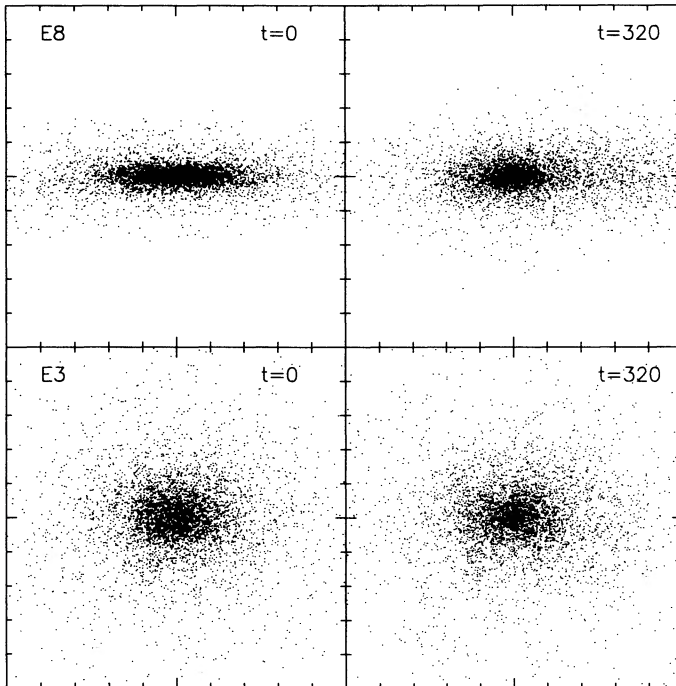


FIG. 13.—Snapshots of the central parts of the E8 and E3 models at initial and final time steps, as evolved with the harmonic-expansion code. Each picture is a projection parallel to the  $y$ -axis; boxes are 10 units square. Ten thousand particles are plotted.

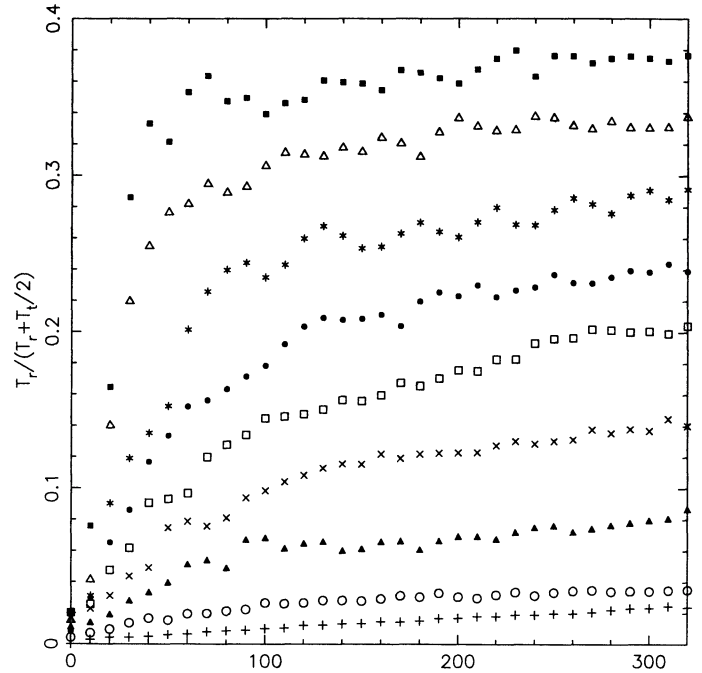


FIG. 14.—Time development of the global velocity anisotropy in each of the 20,000 particle integrations. Crosses: E0 (spherical) model.

roughly, the relation between the final global velocity anisotropy and the initial flattening  $En$  is

$$\frac{2T_r}{2T_r + T_t} \approx \frac{n}{20}, \quad 1 \leq n \leq 8. \quad (13)$$

We also show for comparison in Figure 14 the evolution of the anisotropy for the E0, or spherical, model, which we believe to be stable. The slow, essentially linear increase of  $T_r$  in this model is probably due just to accumulated errors in the orbit integrations.

The internal kinematical structure of the E3 and E8 models is displayed more fully in Figure 15, which shows initial and final velocity dispersion profiles in the prolate-spheroidal coordinate system  $(\lambda, \nu, \phi)$  defined by equations (B2). In this coordinate system, shell orbits in the equilibrium models lie along surfaces of constant  $\lambda$ , which are confocal prolate spheroids; thus  $\sigma_\lambda \equiv 0$  initially. The dispersions in Figure 15 were averaged in bins of constant  $\lambda$ , centered on the grid center; in the equatorial plane,  $\lambda = 1 + \varpi^2$ . Both E8 and E3 models develop nearly isotropic cores, i.e.,  $\sigma_\lambda \approx \sigma_\nu \approx \sigma_\phi$  for  $r \lesssim 0.5$ . In the E8 integration, the final “radial” dispersion  $\sigma_\lambda$  exceeds  $\sigma_\nu$  by a substantial factor at larger radii, although both dispersions remain small compared to  $\sigma_\phi$ . It follows that this model at the final time step is *more* radially anisotropic than an oblate two-integral  $(E, L_2)$  model, for which  $\sigma_\lambda \equiv \sigma_\nu$ . This result suggests (though certainly does not prove) that two-integral models as flat as E8 will be unstable to nonaxisymmetric modes. The E3 model shows substantially less kinematic evolution, with  $\sigma_\lambda \ll \sigma_\nu$  and  $\sigma_\phi$  for  $r \gtrsim 1$ . A two-integral model as round as E3 would therefore probably be stable.

The local velocity distribution in a shell-orbit model is peculiar, since all stars pass through a given point with nearly the same speed, producing a sharply double-peaked distribution of

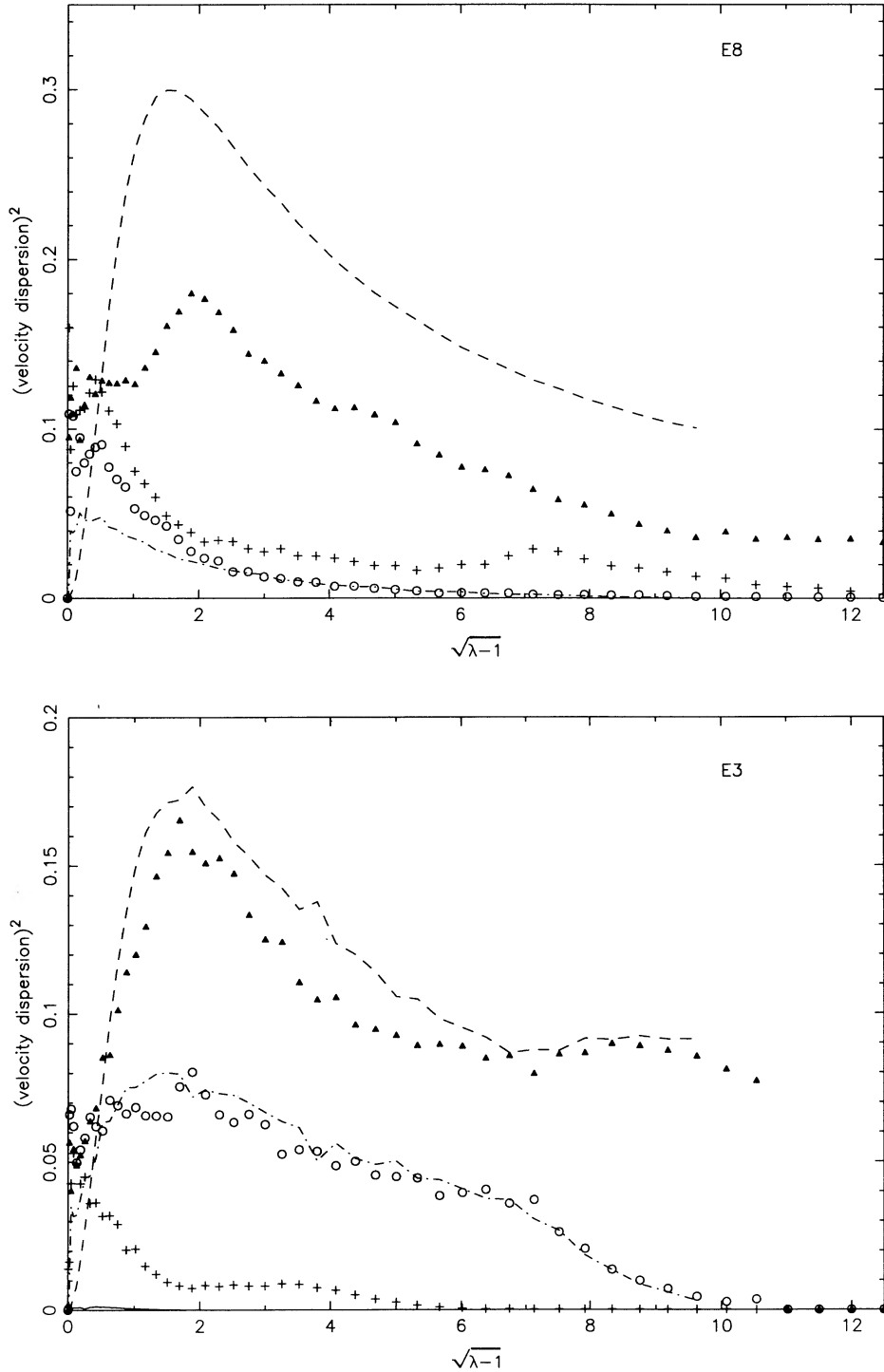


FIG. 15.—Initial (lines) and final (symbols) velocity dispersion profiles for two models, expressed in prolate-spheroidal coordinates. Abscissa is equal to  $\varpi$  for a particle in the equatorial plane. Dashed line triangles:  $\sigma_\phi^2$ ; Dash-dot line, circles:  $\sigma_z^2$ ; Solid line, crosses:  $\sigma_\lambda^2$ .

tangential velocities. Figure 16 shows how this velocity distribution is modified by the nonaxisymmetric evolution. Plotted as a function of  $(\lambda - 1)^{1/2} = \varpi_{z=0}$  is the “tangential” velocity  $v_{\text{tan}} = (v_v^2 + v_\phi^2)^{1/2}$ , i.e., the component of the velocity parallel to the local surface of constant  $\lambda$ . The sign of  $v_{\text{tan}}$  is taken to be the sign of the  $z$ -angular momentum. Clearly the distribution of tangential velocities is greatly broadened in

both models by the instability, although the basic bimodality remains, even near the center. This fact suggests that the “two-stream” character of the local velocity distribution is not inherently unstable. The sharp change in the shape of the velocity distribution near  $\varpi = 5$  in both final models is probably due just to incomplete relaxation; similar features are seen at the same radius in the density profiles (Fig. 12).

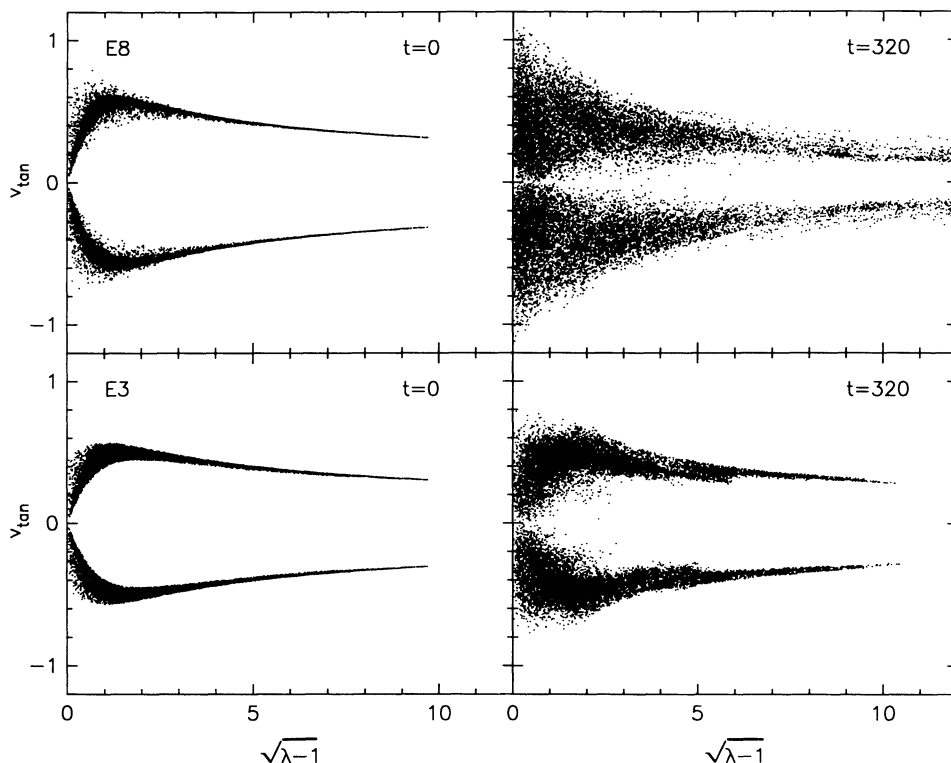


FIG. 16.—Tangential velocities of particles in the E8 and E3, 20,000 particle integrations. Abscissa is equal to  $\varpi$  for a particle in the equatorial plane; ordinate is  $\pm(v_r^2 + v_\phi^2)^{1/2}$ .

#### IV. DISCUSSION

Our results imply that oblate stellar systems, of any flattening (except precisely spherical), require a minimum amount of radial kinetic energy to be dynamically stable, even in the complete absence of rotation, and that the dominant unstable mode has a dipole or “ $m = 1$ ” character. For relatively flat models—say, flatter than E5—the large amounts of evolution seen here suggest that the radial velocity dispersions required for stability may be quite large, of order  $\frac{1}{4}$  to  $\frac{1}{3}$  the circular velocity. For rounder models, the minimum, stable, radial velocity dispersion is less, and the spherical shell-orbit model appears to be stable, at least on time scales no greater than a few orbital periods. It is clearly important to extend these calculations to self-consistent models composed of more general orbits, and to determine the precise ratio of radial to tangential velocity dispersion required for stability as a function of model flattening. Such models have been constructed by Bishop (1986) and Dejonghe and de Zeeuw (1988*b*), among others. Until the results of these calculations are available, we limit ourselves to making the following points about the astrophysical importance of the  $m = 1$  instability in nonrotating oblate systems.

1. *Radially anisotropic, spherical models* are often bar-unstable (Polyachenko and Shukhman 1981; Barnes 1985; Merritt and Aguilar 1985), and there are hints that oblate models with large radial velocity dispersions are likewise unstable (Aguilar and Merritt 1990). It follows that, for any flattening, there is only a limited range of anisotropies—neither too tangential nor too radial—for which an oblate model can be stable. In the case of very flat oblate models, this range could conceivably be narrow, or even nonexistent. Thus we should be able in the future to limit substantially the range

of kinematical solutions consistent with a given model shape, and perhaps even rule out oblate models (in favor of prolate or triaxial ones) with flattenings greater than some limiting ellipticity.

2. Shell-orbit models do not seem very suitable representations of real elliptical galaxies: it is difficult to imagine a formation mechanism that could completely dissipate radial motions without also greatly reducing the tangential velocity dispersion at each radius. Nevertheless, these models have already been invoked in two contexts to explain otherwise puzzling kinematical data (Dejonghe and de Zeeuw 1988*a*; Fillmore and Levison 1989). For instance, Fillmore and Levison (1989) show that, in order for very flattened oblate models to exhibit velocity dispersion profiles that decline with radius along both principal axes, as some observed galaxies do (e.g., Illingworth 1981), the orbits in these models must be fairly thin. Our results show that such flat, radially cold galaxies would very likely be unstable.

3. At the same time, our work suggests that observers should be alert to the possibility of  $m = 1$  deformations in real elliptical galaxies. Most elliptical galaxy isophote fitting is based on the *assumption* that the isophotes are concentric; deviations from elliptical form are then searched for in the higher order harmonics, i.e.,  $m = 2, 3, 4, \dots$ . However, there is at least one elliptical galaxy that is known to show a substantial  $m = 1$  deformation, namely NGC 6487 (R. Bender, private communication). The strong global response of this galaxy (perhaps to a recent encounter with a neighboring galaxy) may indicate that NGC 6487 was formed with a very tangential velocity distribution.

4. Polyachenko (1987) and Palmer, Papaloizou, and Allen (1989) have recently discussed mechanisms for instability of

*spherical* systems constructed from circular or nearly circular orbits. For instance, the latter authors show that spherical systems with small but finite radial velocity dispersions are subject to overstable, quadrupole oscillations which grow on a time scale of tens of crossing times and which gradually increase the central concentration and radial velocity dispersion of the models. While these instabilities, or ones like them, may have important implications for the long-term evolution of elliptical galaxies, the  $m = 1$  instability discovered here afflicts precisely the same sorts of systems, grows on a much shorter time scale, and substantially increases the radial velocity dispersion. Palmer, Paploizou, and Allen failed to see the  $m = 1$  instability because they considered only exactly spherical models and restricted themselves to  $m = 2$  perturbations.

It is important to understand the physical mechanism that drives the  $m = 1$  instability in radially cold, spheroidal systems. The data from the  $N$ -body integrations suggest a picture in which the *centers* of the (nearly circular) orbits move collectively toward one side of the model or the other, producing lopsided density enhancements, while the *orientations* of the orbits remain roughly fixed. Such a picture is consistent with the general appearance of the instability, in particular the weak dependence of its amplitude on  $z$  (e.g., Fig. 9b), and with the fact that the instability seems to grow substantially on a single orbital time scale. In a general way, it is reasonable that such an instability should be strongest in flattened systems: in a spherical model, a shift of any spherical shell produces no

change in the force on interior shells, while in a flattened system, neighboring rings attract one another. A logical first step in understanding the instability in more detail would be to verify that it is indeed active in the linear regime in oblate models, perhaps by applying the adiabatic deformation technique of Binney and May (1986) and Goodman (1988) to the models analyzed here and observing the changes in individual orbits. A second step might be to study analytically the stability of *homogeneous* shell-orbit models (Bisnovaty-Kogan and Zel'dovich 1970), for which the normal modes of oscillation are finite polynomials in the coordinates (Fridman and Polyachenko 1984).

The successful completion of this project would not have been possible without the timely assistance of Lars Hernquist, who graciously lent us a copy of his tree  $N$ -body code and guided us in its implementation. The harmonic-expansion  $N$ -body code used here is a descendant of a code first written by Tjeerd van Albada. Suguru Araki provided us with detailed information on his disk stability calculations. A number of people, including Martin Schwarzschild, Jerry Sellwood, Scott Tremaine, Peter Vandervoort, Tim de Zeeuw, and especially Herwig Dejonghe, examined our  $N$ -body results and made comments that affected the content and organization of this paper. This work was supported in part by a Fullam/Dudley Award from the Dudley Observatory.

## APPENDIX A

### REDUCTION FACTOR FOR OBLATE MODELS

Following Shu (1968) and Vandervoort (1970), we derive here a heuristic reduction factor by assuming that an unstable oblate model laminates into thin cylinders whose density, in the linear regime, is proportional to the unperturbed density at any point  $z$  above the equatorial plane. The density perturbation is then the real part of

$$\rho_1(\varpi, z)e^{i(k\varpi - \omega t)} = \frac{\Sigma_1(\varpi)}{\Sigma(\varpi)} \rho(\varpi, z)e^{i(k\varpi - \omega t)}, \quad (\text{A1})$$

where  $\Sigma(\varpi)$  and  $\rho(\varpi)$  are the unperturbed surface and volume densities and  $\Sigma_1(\varpi) = \int_{-\infty}^{\infty} dz \rho_1(\varpi, z)$ . The perturbed potential corresponding to the assumed density perturbation is  $\Phi_1(\varpi, z)e^{i(k\varpi - \omega t)}$ , where, from Poisson's equation,

$$\Phi_1(\varpi, z) \approx -\frac{2\pi G}{k} \frac{\Sigma_1(\varpi)}{\Sigma(\varpi)} \int_{-\infty}^{\infty} e^{-k|z-z'|} \rho(\varpi, z') dz'. \quad (\text{A2})$$

To obtain a dispersion relation, we need a second expression that gives the density response to the imposed potential. For an infinitely thin, cold disk, this relation is

$$\Sigma_1(\varpi) = -\frac{k^2}{\kappa^2 - \omega^2} \Sigma(\varpi) \Phi_1(\varpi) \quad (\text{A3})$$

(e.g., Kalnajs 1965). In the present case, we assume that the response density is simply

$$\rho_1(\varpi, z) \approx -\frac{k^2}{\kappa^2 - \omega^2} \rho(\varpi, z) \langle \Phi_1(\varpi, z) \rangle_z, \quad (\text{A4})$$

where the angle brackets indicate some average over  $z$ ; this average reflects the fact that stars contributing to the perturbed density at  $z$  feel the perturbed potential at a range of different heights above the equatorial plane. To be consistent with our assumption that  $\rho_1$  values have the same  $z$ -dependence as  $\rho$ , this average must be independent of  $z$ ; we assume

$$\langle \Phi_1(\varpi, z) \rangle_z = \frac{1}{\Sigma(\varpi)} \int_{-\infty}^{\infty} dz \rho(\varpi, z) \Phi_1(\varpi, z). \quad (\text{A5})$$

The weighting with  $\rho$  is reasonable, since the time that a star spends in the vicinity of  $z$  is proportional to the unperturbed density there.

Equating the imposed and response densities then gives an approximate dispersion relation for axisymmetric oscillations of a shell-orbit model:

$$\omega^2 = \kappa^2 - \frac{2\pi Gk}{\Sigma(\varpi)} \int_{-\infty}^{\infty} \int_{-\infty}^{\infty} \rho(\varpi, z)\rho(\varpi, z')e^{-k|z-z'|} dz dz'. \quad (\text{A6})$$

As in the case of a razor-thin disk, equation (A6) predicts that the shortest wavelength oscillations are the most unstable. In the limit  $k \rightarrow \infty$ , equation (A6) becomes

$$\omega^2 = \kappa^2 - 4\pi G \frac{\int_0^{\infty} \rho^2(\varpi, z) dz}{\int_0^{\infty} \rho(\varpi, z) dz}, \quad (\text{A7a})$$

$$= \kappa^2 - 4\pi G \langle \rho(\varpi, z) \rangle_z. \quad (\text{A7b})$$

## APPENDIX B

### INITIAL COORDINATES

Generation of initial conditions for the  $N$ -body code required, first, numerical computation of the orbital distribution function; and, second, Monte-Carlo calculation of positions and velocities. Computation of the distribution function was carried out according to the prescription of Bishop (1987) (with one minor modification, described below). To maintain consistency with more recent work, we present the basic equation (B7) also in the notation of de Zeeuw and Hunter (1990).

In prolate spheroidal coordinates  $(\lambda, \nu, \phi)$ , the Kuzmin-de Zeeuw oblate-spheroidal mass distribution (1) becomes

$$\rho(\lambda, \nu) = \frac{c^3}{\pi^2} \frac{1}{\lambda^2 \nu^2} \quad (\text{B1})$$

where

$$x^2 + y^2 \equiv \varpi^2 = \frac{(\lambda - 1)(1 - \nu)}{1 - c^2}, \quad z^2 = \frac{(\lambda - c^2)(\nu - c^2)}{1 - c^2}, \quad c^2 \leq \nu \leq 1 \leq \lambda, \quad (\text{B2})$$

in units such that  $a = \text{total mass} = 1$ . The potential is

$$V(\lambda, \nu) = - \frac{(\lambda - c^2)G(\lambda) - (\nu - c^2)G(\nu)}{\lambda - \nu}, \quad G(\tau) = \frac{2}{\pi} (\tau - c^2)^{-1/2} \tan^{-1} \sqrt{\frac{\tau - c^2}{c^2}}, \quad (\text{B3})$$

where the gravitational constant has also been set to unity. "Shell" orbits lie along surfaces defined by

$$\lambda = \lambda_1, \quad c^2 \leq \nu \leq \nu_0, \quad 0 \leq \phi \leq 2\pi. \quad (\text{B4})$$

Let  $n(\lambda_1, \nu_0)d\lambda_1 d\nu_0$  be the mass of stars with turning points  $(\lambda_1, \nu_0)$  in the annulus between  $(\lambda_1, \nu_0)$  and  $(\lambda_1 + d\lambda_1, \nu_0 + d\nu_0)$ . The distribution of orbital parameters that reproduces the density profile (B1) in the potential (B3) is

$$n(\lambda_1, \nu_0) = - T(\lambda_1, \nu_0) \frac{\partial \mathcal{P}}{\partial \nu_0}, \quad (\text{B5})$$

where  $T = 4 \int_c^{\nu_0} d\nu / |\dot{\nu}|$  is the period of a complete oscillation in  $\nu$ ,

$$\mathcal{P}(\lambda_1, \nu_0) = \frac{1}{\pi} \int_0^{\nu_0} \frac{\mathcal{R}(\lambda_1, y)}{\sqrt{y_0 - y}} dy, \quad (\text{B6a})$$

$$\mathcal{R}(\lambda_1, \nu) = \frac{\pi}{2} \frac{(\lambda_1 - \nu)}{\sqrt{\lambda_1 - c^2}(\lambda_1 - 1)} \rho(\lambda_1, \nu), \quad (\text{B6b})$$

and

$$y = \mathcal{L}_z^2(\lambda_1, \nu) = - \frac{2(\lambda_1 - 1)^2(1 - \nu)}{(1 - c^2)(\lambda_1 - \nu)} \left[ V(\lambda_1, \nu) + \frac{G(\lambda_1)}{2} + \frac{c}{\pi\lambda_1} \right]; \quad (\text{B6c})$$

$y_0 = \mathcal{L}_z^2(\lambda_1, \nu_0) = L_z^2$ , the  $z$ -angular momentum of an orbit with turning point  $(\lambda_1, \nu_0)$  (Bishop 1987). In the notation of de Zeeuw and Hunter (1990),

$$n(\lambda_1, \nu_0) = \frac{\pi}{\sqrt{2(1 - c^2)(\lambda_1 - c^2)}} T(\lambda_1, \nu_0) F_{\text{ism}}^*(\lambda_1, \nu_0), \quad (\text{B7})$$

where  $F_{\text{tsm}}^*(\lambda_1, v_0)$  is expressed elegantly in terms of “divided differences” by their equation (2.32). Equations (B5)–(B6) were solved numerically.

Given  $n(\lambda_1, v_0)$ , we can generate initial coordinates and velocities for the  $N$ -body code as follows. The cumulative distribution of the “radial” coordinate  $\lambda_1$  is

$$N(<\lambda_1) = \int_{\lambda_1}^{\lambda_1} \int_{c^2}^1 \int_0^{2\pi} \rho(\lambda_1, v) \frac{\partial(x, y, z)}{\partial(\lambda_1, v, \phi)} d\lambda_1 dv d\phi \quad (\text{B8a})$$

$$= \frac{2}{\pi} \left( \tan^{-1} \sqrt{\frac{\lambda_1 - c^2}{c^2}} - \frac{1}{\lambda_1} \sqrt{\frac{\lambda_1 - c^2}{1 - c^2}} \tan^{-1} \sqrt{\frac{1 - c^2}{c^2}} \right). \quad (\text{B8b})$$

Given a value for  $\lambda_1$ , the cumulative distribution of  $v_0$  is

$$N(<v_0; \lambda_1) = \int_{c^2}^{v_0} n(\lambda_1, v_0) dv_0, \quad (\text{B9a})$$

$$= T(\lambda_1, c^2) \mathcal{P}(\lambda_1, c^2) - T(\lambda_1, v_0) \mathcal{P}(\lambda_1, v_0) + \int_{c^2}^{v_0} \frac{\partial T}{\partial v_0} \mathcal{P}(\lambda_1, v_0) dv_0. \quad (\text{B9b})$$

The fraction of stars with turning points  $(\lambda_1, v_0)$  that lie between  $v$  and  $v + dv$  at any instant is  $2/|\dot{v}| T(\lambda_1, v_0)$ ; thus the cumulative distribution of  $v$  for a given  $(\lambda_1, v_0)$  is

$$N(<v; \lambda_1, v_0) = \frac{2}{T(\lambda_1, v_0)} \int_{c^2}^v \frac{dv}{|\dot{v}|}, \quad v < v_0, \quad (\text{B10})$$

where

$$\dot{v}(v; \lambda_1, v_0) = \pm 2 \frac{\sqrt{(1 - c^2)(v - c^2)}}{(\lambda_1 - 1)} \sqrt{\mathcal{L}_z^2(\lambda_1, v) - \mathcal{L}_z^2(\lambda_1, v_0)}. \quad (\text{B11})$$

The cylindrical velocity components are then

$$\dot{\omega} = - \frac{\lambda_1 - 1}{2(1 - c^2)} \frac{\dot{v}}{\omega}, \quad (\text{B12a})$$

$$\dot{z} = \frac{\lambda_1 - c^2}{2(1 - c^2)} \frac{\dot{v}}{z}, \quad (\text{B12b})$$

$$\omega\phi = \pm \frac{\lambda_1 - 1}{\omega} \left\{ \frac{2(1 - v_0)}{(1 - c^2)(\lambda_1 - v_0)} \left[ -G(\lambda_1) - (\lambda_1 - c^2) \frac{dG}{d\lambda_1} - V(\lambda_1, v_0) \right] \right\}^{1/2}. \quad (\text{B12c})$$

Equations (B6)–(B8) apply to a model with infinite extent. For the purposes of the  $N$ -body code, which evaluates forces on a finite grid, we required a finite model. The simplest way to modify the infinite model is to truncate it on a surface of constant  $\tilde{m}^2 = \tilde{m}_0^2$ ; doing so leaves the interior force field and the particle equations of motion intact. In terms of  $\lambda$  and  $v$ , the truncation surface is defined by

$$c^2 \leq v \leq 1, \quad 1 \leq \lambda \leq c^2 \tilde{m}_0^2;$$

$$c^2 \leq v \leq v_{\text{max}}(\lambda), \quad c^2 \tilde{m}_0^2 \leq \lambda \leq \tilde{m}_0^2,$$

where  $v_{\text{max}}(\lambda) = c^2 \tilde{m}_0^2 / \lambda$ . Since shell orbits of a given  $\lambda_1$  can extend all the way to  $v = 1$ , it is clear that the orbital distribution of the truncated model must be adjusted to include only orbits that remain inside the truncation surface. It is easy to show that  $\mathcal{P}$  for the truncated model is

$$\mathcal{P}_{\text{trun}}(\lambda_1, v_0) = \frac{1}{\pi} \int_{y_{\text{min}}}^{y_0} \frac{\mathcal{R}(\lambda_1, y)}{\sqrt{y_0 - y}} dy \quad v_0 \leq v_{\text{max}}(\lambda_1), \quad (\text{B13a})$$

$$= 0 \quad v_0 > v_{\text{max}}(\lambda_1), \quad (\text{B13b})$$

where  $y_{\text{min}} = \mathcal{L}_z^2[\lambda_1, v_{\text{max}}(\lambda_1)]$ . Because of the sharp truncation, the orbital distribution of the truncated model is divergent at  $v = v_{\text{max}}(\lambda)$  for  $\lambda_1 > c^2 \tilde{m}_0^2$ . However the cumulative distribution  $N(<v_0; \lambda_1)$ , which is the important quantity from the point of view of generating initial coordinates and velocities, remains well behaved (see eq. [B9b]).

#### REFERENCES

- Aguilar, L. A., and Merritt, D. 1990, *Ap. J.*, **354**, 33.  
 Antonov, V. A. 1960, *Astr. Zh.*, **37**, 918.  
 ———. 1962, *Vestnik Leningrad Univ.*, **19**, 96.  
 Araki, S. 1987, *A.J.*, **94**, 99.  
 Barnes, J. 1985, in *IAU Symposium 114, Dynamics of Star Clusters*, ed. J. Goodman and P. Hut (Dordrecht: Reidel), p. 297.  
 Barnes, J., Goodman, J., and Hut, P. 1986, *Ap. J.*, **300**, 112.  
 Bertin, G., and Stiavelli, M. 1989, *Ap. J.*, **338**, 723.

- Binney, J. J. 1987, in *IAU Symposium 127, Structure and Dynamics of Elliptical Galaxies*, ed. T. de Zeeuw (Dordrecht: Reidel), p. 229.
- Binney, J. J., and May, A. 1986, *M.N.R.A.S.*, **221**, 13p.
- Bishop, J. L. 1986, *Ap. J.*, **305**, 14.
- . 1987, *Ap. J.*, **322**, 618.
- . 1988, in *Proc. 2d Canadian Conference on General Relativity and Relativistic Astrophysics*, ed. A. Coley, C. Dyer and T. Tupper (Singapore: World Scientific), p. 339.
- Bishop, J. L., Duncan, M., and Lee, M. H. 1987, unpublished.
- Bisnovatyi-Kogan, G. S. 1971, *Astrofizika*, **7**, 223.
- Bisnovatyi-Kogan, G. S., and Zel'dovich, Ya. B. 1970, *Astrofizika*, **6**, 387.
- Bisnovatyi-Kogan, G. S., Zel'dovich, Ya. B., and Fridman, A. M. 1968, *Dokl. Akad. Nauk SSSR*, **182**, 794.
- Bontekoe, T. R. 1988, Ph.D. thesis, Groningen University.
- Dejonghe, H. 1986, *Phys. Rept.*, **133**, 217.
- . 1987, in *IAU Symposium 127, Structure and Dynamics of Elliptical Galaxies*, ed. T. de Zeeuw (Dordrecht: Reidel), p. 495.
- Dejonghe, H., and de Zeeuw, T. 1988a, *Ap. J.*, **329**, 720.
- . 1988b, *Ap. J.*, **333**, 90.
- Dejonghe, H., and Merritt, D. 1988, *Ap. J.*, **328**, 93.
- de Zeeuw, T. 1985, *M.N.R.A.S.*, **216**, 273.
- de Zeeuw, T., Franx, M., Meys, J., Brink, K., and Habing, H. 1983, in *IAU Symposium 100, Internal Kinematics and Dynamics of Galaxies*, ed. E. Athanassoula (Dordrecht: Reidel), p. 285.
- de Zeeuw, T., and Hunter, C. 1990, preprint.
- Evans, N. W. 1989, Ph.D. thesis, Cambridge University.
- Fillmore, J. A., and Levison, H. F. 1989, *A.J.*, **97**, 57.
- Fridman, A. M., and Polyachenko, V. L. 1984, *Physics of Gravitating Systems* (New York: Springer).
- Goodman, J. 1988, *Ap. J.*, **329**, 612.
- Hernquist, L. 1987, *Ap. J. Suppl.*, **64**, 715.
- Hori, G. 1962, *Pub. Astr. Soc. Japan*, **14**, 353.
- Illingworth, G. 1981, in *The Structure and Evolution of Normal Galaxies*, ed. S. M. Fall and D. Lynden-Bell (Cambridge: Cambridge University Press), p. 27.
- Kalnajs, A. 1965, Ph.D. Thesis, Harvard University.
- . 1972, *Ap. J.*, **175**, 63.
- . 1977, *Ap. J.*, **212**, 637.
- Kuzmin, G. G. 1956, *Astr. Zh.*, **33**, 27.
- Lin, C. C., and Shu, F. H. 1966, *Proc. Nat. Acad. Sci.*, **55**, 229.
- Merritt, D., and Aguilar, L. A. 1985, *M.N.R.A.S.*, **217**, 787.
- Meys, J. J. M. 1981, M.Sc. thesis, Leiden University.
- Mikhailovskii, A. B., Fridman, A. M., and Epelbaum, Ya. G. 1971, *Soviet Phys.—JETP*, **32**, 878.
- Palmer, P. L., Papaloizou, J., and Allen, T. 1989, *M.N.R.A.S.*, **238**, 1281.
- Polyachenko, V. L. 1987, in *IAU Symposium 127, Structure and Dynamics of Elliptical Galaxies*, ed. T. de Zeeuw (Dordrecht: Reidel), p. 301.
- Polyachenko, V. L., and Shukhman, I. G. 1981, *Astr. Zh.*, **58**, 933.
- Richstone, D. O. 1982, *Ap. J.*, **252**, 496.
- Sellwood, J. A. 1987, *Ann. Rev. Astr. Ap.*, **25**, 151.
- Shapiro, S. L., and Teukolsky, S. A. 1987, *Ap. J.*, **318**, 542.
- Shu, F. H. 1968, Ph.D. thesis, Harvard University.
- . 1969, *Ap. J.*, **158**, 505.
- Shukhman, I. G. 1973, *Astr. Zh.*, **50**, 651.
- Stäckel, P. 1890, *Math. Ann.*, **35**, 91.
- Synakh, V. S., Fridman, A. M., and Shukhman, I. G. 1972, *Astrofizika*, **8**, 577.
- Toomre, A. 1964, *Ap. J.*, **139**, 1217.
- van Albada, T. S. 1982, *M.N.R.A.S.*, **201**, 939.
- van Albada, T. S., and van Gorkom, J. H. 1977, *Astr. Ap.*, **54**, 121.
- Vandervoort, P. O. 1970, *Ap. J.*, **161**, 87.
- Zang, T. A., and Hohl, F. 1978, *Ap. J.*, **226**, 521.

DAVID MERRITT: Department of Physics and Astronomy, Rutgers University, Serin Physics Labs, Piscataway, NJ 08855

MASSIMO STIAVELLI: European Southern Observatory, D-8046 Garching bei München, Federal Republic of Germany